

# Central molecular zones in galaxies: Multitransition survey of dense gas tracers HCN, HNC, and HCO<sup>+</sup>

F.P. Israel<sup>1</sup>

Leiden Observatory, Leiden University, P.O. Box 9513, 2300 RA Leiden, the Netherlands

Received ????: accepted ????

## ABSTRACT

New measurements of 46 nearby galaxy centers in up to three transitions of HCN, HNC, and HCO<sup>+</sup> combined with literature surveys establish a database of 130 galaxies measured in both HCN and HCO<sup>+</sup>, and 94 galaxies in HNC as well, allowing a systematic exploration of the relations between normalized luminosities and line ratios. The almost linear relations between luminosities are predominantly caused by distance effects and do not reflect galaxy physical properties. Individual galaxies show significant dispersion in both their luminosity and line ratio, which will be analyzed in more detail in a later paper. Very few line ratios correlate either with luminosities or with other line ratios. Only the normalized transition ladders of HCN and HCO<sup>+</sup> and the  $J=1-0$  <sup>12</sup>CO/<sup>13</sup>CO isotopologue ratio are positively correlated with CO and far infrared (FIR) luminosity. On average, HCN and HCO<sup>+</sup> have very similar intensities and trace the same gas. In galaxies dominated by an active nucleus, HCO<sup>+</sup> intensities appear to be depressed relative to HCN intensities. Only a small fraction of CO emission is associated with gas emitting in HCN and HCO<sup>+</sup>, yet a significant fraction of even that gas appears to be translucent molecular gas. In the observed galaxy centers, the HCN/CO line intensity ratio is not a proxy for the dense gas fraction, and the FIR/HCN and FIR/CO ratios are not proxies for the star formation efficiency. A proper understanding of star formation requires a more appropriate determination of gas mass than provided by the intensities of individual HCN or CO transitions. The observed molecular line emission is fully consistent with UV-photon heating boosted by significant mechanical heating. The molecular gas sampled by HCN and HCO<sup>+</sup> has low kinetic temperatures  $T_{\text{kin}} = 10 - 50$  K, low densities  $n_{\text{rnh}} = 10^4 - 10^5$  cm<sup>-3</sup>, and low optical depths in the ground-state lines. Most of the gas sampled by CO has densities lower by one to two orders of magnitude. For a mechanical heating fraction of 0.5, a modest energy input of only  $G = 300$  G<sub>0</sub> is required.

**Key words.** Galaxies: galaxies: centers – interstellar medium: molecules – millimeter lines – observations

## 1. Introduction

This paper presents multitransition measurements of the HCN, HNC and HCO<sup>+</sup> molecular species tracing the dense molecular gas in the centers of nearby galaxies. Many late-type galaxies contain massive concentrations of molecular hydrogen gas close to the nucleus. These concentrations form the reservoirs that feed mass inflow into supermassive black holes (SMBH), mass outflow from the nucleus into space, and bursts of circumnuclear star formation. In a previous paper (Israel 2020), we have explored the physical characteristics of the inner-disk gas from measurements of the lower  $J$  transitions of <sup>12</sup>CO and <sup>13</sup>CO, augmented by literature measurements of neutral ([CI]) and ionized ([CII]) atomic carbon.

Gas inflow and outflow involve both dense clouds and diffuse intercloud gas together responsible for the carbon and carbon monoxide emission studied in that paper. Star formation, in contrast, is exclusively associated with the dense gas. The determination of the properties of that gas requires observation of molecules that, unlike CO, need relatively high densities for excitation at modest temperatures. Molecules such as HCN, HCO<sup>+</sup>, HNC, and CS are suitable for this purpose even though they have abundances much lower than CO and much weaker emission lines. In Table 1 we list, for these molecules in the relevant transitions, the line frequency, the minimum temperature for excitation  $T_{\text{min}} = E_{\text{upper}}/k$ , and the temperature-dependent critical density  $n_{\text{crit}}$  for an assumed kinetic temperature  $T_{\text{kin}} =$

**Table 1.** Critical densities

| Molecule<br>(1)  | Transition<br>(2) | Frequency<br>(GHz)<br>(3) | $E_u/k^a$<br>(K)<br>(4) | $n_{\text{crit}}^{a,b}$<br>(cm <sup>-3</sup> )<br>(5) | $n_{\text{eff}}^c$<br>(cm <sup>-3</sup> )<br>(6) |
|------------------|-------------------|---------------------------|-------------------------|---|--|
| CO               | 1-0               | 115.271                   | 5.5                     | 4 (2)   | ...  |
|                  | 2-1               | 230.538                   | 16.6                    | 5 (3)   | ...  |
|                  | 3-2               | 345.796                   | 33.2                    | 2 (4)   | ...  |
|                  | 4-3               | 461.041                   | 55.3                    | 2 (5)   | ...  |
| HCN              | 1-0               | 88.632                    | 4.3                     | 2 (5)   | 3 (3)  |
|                  | 3-2               | 265.886                   | 25.5                    | 8 (6)   | 1 (4)  |
|                  | 4-3               | 354.506                   | 42.5                    | 2 (7)   | 2 (5)  |
| HCO <sup>+</sup> | 1-0               | 89.189                    | 4.3                     | 3 (4)   | 4 (2)  |
|                  | 3-2               | 267.558                   | 25.7                    | 1 (6)   | 4 (3)  |
|                  | 4-3               | 356.734                   | 42.8                    | 3 (6)   | 2 (4)  |
| HNC              | 1-0               | 90.664                    | 4.4                     | 1 (5)   | 2 (3)  |
|                  | 3-2               | 271.981                   | 26.1                    | 4 (6)   | 3 (4)  |
|                  | 4-3               | 362.630                   | 43.5                    | 9 (6)   | 1 (5)  |
| C <sub>2</sub> H | 1-0               | 87.317                    | 4.3                     | 2 (5)   | 2 (4)  |
| CS               | 2-1               | 97.981                    | 7.1                     | 9 (4)   | 9 (3)  |
|                  | 3-2               | 146.969                   | 14.1                    | 3 (5)   | 3 (4)  |

Notes: a. Jansen (1995) and Shirley (2015); b. Calculated for  $T_{\text{kin}} = 30$  K in the optically thin limit; c. Shirley (2015), with  $\log N_{\text{ref}} = 14.0$  (HCN, HCO<sup>+</sup>, and HNC) and  $\log N_{\text{ref}} = 13.5$  (CS, C<sub>2</sub>H)

30 K (cf. Paper I). Critical densities are lower for warmer gas and higher for cooler gas, roughly by factors of up to two going from 30 K to either 10 K or 100 K and HCN traces the highest densities. As molecular emission remains detectable, however, at densities well below  $n_{crit}$ , we also list the effective de-excitation density  $n_{eff}$ . Somewhat arbitrarily, this is the density that produces a line of intensity  $1 \text{ K km s}^{-1}$ , for a given temperature and column density (see Evans 1999; Shirley 2015). The molecules and transitions in Table 1 cover a wide range of excitation conditions, including densities  $10^2 - 10^7 \text{ cm}^{-3}$  and temperatures 4–55 K. In their study of molecular cloud ensembles in the inner Galaxy, Evans et al. (2020) found that the integrated HCN and  $\text{HCO}^+$  luminosity can be dominated by emission from even more tenuous molecular gas with densities as low as  $10^2 \text{ cm}^{-3}$ .

After the brightest individual galaxies had been observed in the relatively accessible  $J=1-0$  lines of HCN,  $\text{HCO}^+$ , and HNC, the first surveys with the *IRAM* 30m telescope, encompassing some fifteen galaxies, were published by Nguyen-Q-Rieu et al. (1992) and Hüttemeister et al. (1995). Among early observations carried out between 1993 and 1997, the large HCN and CO survey of 53 galaxies by Gao & Solomon (2004a) and the survey of 37 galaxies in HCN, HNC,  $\text{HCO}^+$ , CO, CN, and CS by Baan et al. (2008) stand out. The latter combined all observations available at the time into a heterogeneous database of 117 galaxies with 23 galaxies detected in all three lines, HCN(1-0), HNC(1-0), and  $\text{HCO}^+(1-0)$ . They concluded that the emission from these lines and the far-infrared (FIR) continuum are tightly correlated, and suggested that the ratio of the HCN-to-CO luminosity traces the fraction of dense molecular gas. Kohno et al. (2001, 2008) and Imanishi et al. (2007) then suggested that the ground-state CO-HCN- $\text{HCO}^+$  line intensity ratios from galaxy centers dominated by a burst of star-formation (SB) differ from those of galaxy centers dominated by nuclear activity (AGN). In their multi-transition *IRAM* 30m survey of the HCN and  $\text{HCO}^+$  emission from a dozen galaxies, Krips et al. (2008) found higher average molecular gas densities in SB galaxies and higher average temperatures and HCN/ $\text{HCO}^+$  line ratios in AGN galaxies. An HCN/ $\text{HCO}^+$  overabundance was, however, also found in luminous (LIRG) and ultra-luminous (ULIRG) galaxies representing extreme SBs (Graciá-Carpo et al. 2008). Bussman et al. (2008) conducted a survey of HCN(3-2) emission and found it to behave differently from HCN(1-0). The major study of dense gas in luminous galaxies by Baan et al. (2008) referred to earlier took these results a step further by constructing diagnostic diagrams to investigate source differentiation as a function of initial conditions and radiative environment.

More recently, the installation of very sensitive multi-mixer receivers (EMIR) with very wide back-end coverage (FTS, WILMA) at the *IRAM* 30m telescope has enormously expanded the possibilities for extra-galactic molecular line measurements as illustrated, for instance, by the spectral scans published by Costagliola et al. (2011) and Jiang et al. (2011). Later in this paper we will refer to their findings as well as those of others obtained since then. We will do this in the context of analyzing and discussing an extensive and homogeneous database of HCN, HNC,  $\text{HCO}^+$ , and CO line intensities in various transitions encompassing the newly obtained observations as well as directly comparable data from the published literature. The database will be used to investigate the overall relations between the various lines and transitions, including verification of previous claims. Detailed modelling of the results is deferred to a later paper.

This paper is structured as follows. Section 2 presents the new observations. Section 3 describes the expansion of the database with line intensities from surveys published by others

**Table 2.** List of observed galaxy centers

| NGC<br>IC<br>(1)   | Dist.<br>(Mpc)<br>(2) | $\lg I_{FIR}$<br>( $\text{W m}^{-2}$ )<br>(3) | $\lg L_{FIR}$<br>( $L_{\odot}$ )<br>(4) | $I_{CO(1-0)}$<br>( $\text{K km/s}$ )<br>(5) | $D_{25}$<br>( $'$ )<br>(6) | Type <sup>a</sup><br>(7) |
|--------------------|-----------------------|---|---|---|----------------------------|--------------------------|
| N 253              | 3.4                   | -10.42  | 10.13                                   | 1030  | 25x7.4                     | S                        |
| N 470              | 31.7                  | -12.44  | 10.04                                   | 28  | 2.8x1.7                    | S                        |
| N 520              | 30.5                  | -11.79  | 10.66                                   | 113   | 4.5x1.8                    | S                        |
| N 660              | 12.2                  | -11.46  | 10.20                                   | 154   | 9.1                        | S                        |
| N 891              | 9.4                   | -11.53  | 9.90                                    | 137   | 14x2.5                     | (S)                      |
| N 972              | 21.4                  | -11.75  | 10.39                                   | 67  | 3.4x1.7                    | S                        |
| Maff2              | 3.1                   | -11.23  | 9.23                                    | 220   | 5.8x1.6                    | S                        |
| N1055              | 13.4                  | -11.84  | 9.89                                    | 77  | 7.6x2.7                    | S                        |
| N1068 <sup>b</sup> | 15.2                  | -11.04  | 10.80                                   | 168   | 7.1x6.0                    | A                        |
| N1084              | 18.6                  | -12.33  | 9.69                                    | 30  | 3.3x1.2                    | (S)                      |
| N1097 <sup>b</sup> | 16.5                  | -11.81  | 10.10                                   | 136   | 9.3x6.6                    | A+S                      |
| N1365 <sup>b</sup> | 21.5                  | -11.36  | 10.78                                   | 260   | 11x6.2                     | A+S                      |
| I342               | 3.8                   | -11.36  | 9.28                                    | 161   | 21x21                      | S                        |
| N1808              | 12.3                  | -11.31  | 10.35                                   | 135   | 6.5x3.9                    | A                        |
| N2146              | 16.7                  | -11.16  | 10.77                                   | 187   | 6.0x3.4                    | S                        |
| N2559              | 21.4                  | -11.78  | 10.36                                   | 78  | 4.1x2.1                    | ...                      |
| N2623              | 79.4                  | -11.94  | 11.34                                   | 18  | 2.4x0.7                    | L                        |
| N2903              | 7.3                   | -11.65  | 9.56                                    | 80  | 13x6.0                     | S                        |
| N3034              | 5.9                   | -10.28  | 10.74                                   | 680   | 11x4.3                     | S                        |
| N3079 <sup>b</sup> | 20.7                  | -11.60  | 10.51                                   | 235   | 7.9x1.4                    | A                        |
| N3310              | 19.2                  | -11.79  | 10.26                                   | 7   | 3.1x2.4                    | S                        |
| N3627              | 6.5                   | -11.61  | 9.50                                    | 74  | 9.1x4.2                    | A+S                      |
| N3628              | 8.5                   | -11.54  | 9.80                                    | 203   | 15x3.0                     | S                        |
| N3690              | 48.5                  | -11.32  | 11.53                                   | 69  | 2.9x2.1                    | L                        |
| N4030              | 26.4                  | -11.95  | 10.37                                   | 42  | 4.3                        | ...                      |
| N4038              | 23.3                  | -11.65  | 10.56                                   | 47  | 5.2x3.1                    | S                        |
| N4102              | 17.3                  | -11.62  | 10.34                                   | 75  | 2.8x1.2                    | A                        |
| N4321              | 14.1                  | -11.88  | 9.90                                    | 82  | 7.4x6.3                    | S                        |
| N4414              | 9.0                   | -11.77  | 9.62                                    | 51  | 3.6x2.0                    | A?                       |
| N4527              | 13.5                  | -11.79  | 9.95                                    | 88  | 6.2x2.1                    | S?                       |
| N4569              | 12.3                  | -12.19  | 9.47                                    | 89  | 9.5x4.4                    | A+S                      |
| N4666              | 27.5                  | -11.74  | 10.62                                   | 74  | 4.6x1.3                    | S                        |
| N4826 <sup>b</sup> | 3.8                   | -11.66  | 9.34                                    | 91  | 10x5.4                     | A+S                      |
| N5033 <sup>b</sup> | 17.2                  | -12.00  | 9.95                                    | 53  | 11x5.0                     | A                        |
| N5055              | 8.3                   | -11.66  | 9.66                                    | 70  | 13x7.2                     | (A)                      |
| N5194 <sup>b</sup> | 9.1                   | -11.59  | 9.81                                    | 48  | 11x6.9                     | A                        |
| N5236              | 4.0                   | -11.22  | 9.46                                    | 195   | 13x12                      | S                        |
| N5775              | 28.9                  | -11.97  | 10.43                                   | 48  | 4.2x1.0                    | ...                      |
| N6240              | 109                   | -11.96  | 11.59                                   | 70  | 2.1x1.1                    | L                        |
| N6701              | 59.1                  | -12.23  | 10.80                                   | 45  | 1.5x1.3                    | A+S                      |
| N6946              | 5.5                   | -11.06  | 9.90                                    | 228   | 11.5x9.8                   | S                        |
| N6951 <sup>b</sup> | 24.3                  | -12.04  | 10.21                                   | 50  | 3.9x3.2                    | A+S                      |
| N7469*             | 67.0                  | -11.88  | 11.25                                   | 55  | 1.5x1.1                    | L                        |
| N7714              | 38.5                  | -12.30  | 10.35                                   | 4   | 1.9x1.4                    | S                        |
| N7771              | 58.0                  | -11.97  | 11.04                                   | 100   | 2.5x1.0                    | L                        |
| Arp220             | 82.9                  | -11.31  | 12.04                                   | 110   | 1.5x1.2                    | U                        |

Notes: a. S = Starburst, A = AGN, L = LIRG, U = ULIRG; parentheses indicate marginal case. b. Seyfert nucleus.

and the normalization applied to data observed at different resolutions in order to obtain a homogeneous sample of intercomparable intensities. Section 4 systematically analyzes the trends and correlations, either present or absent, between the various observed line intensities and line ratios. Section 5 discusses the meaning of these findings. Section 6 summarizes the most important points.

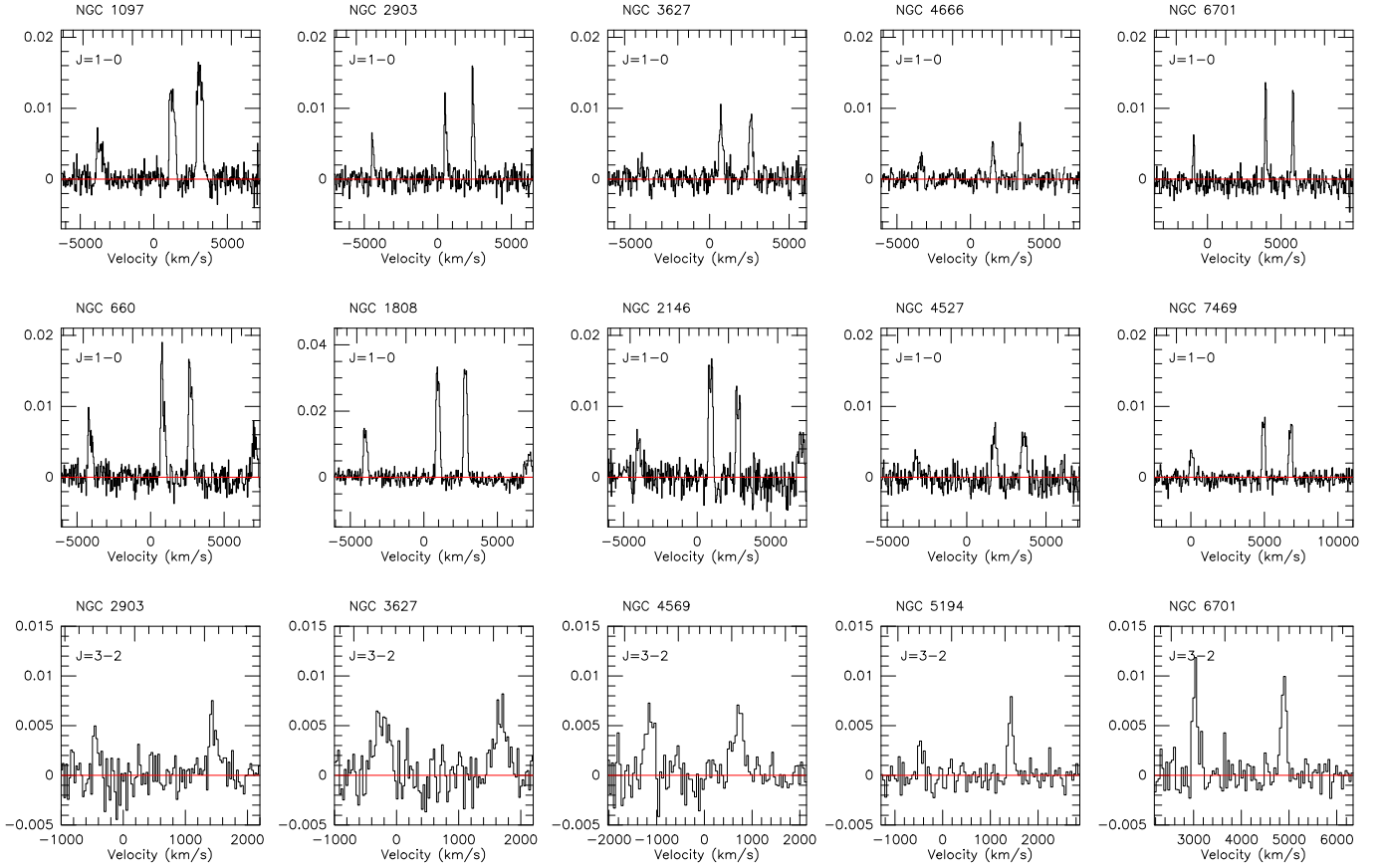


**Fig. 1.** Sample of molecular line profiles of galaxy centers observed with the *IRAM* 30m telescope. Galaxy and transition depicted are identified at the top of each panel. The top row shows  $J=1-0$  observations of (in each panel from left to right) HNC, HCO<sup>+</sup>, and HCN observed in 2010. The middle row shows the same lines and includes the C<sub>2</sub>H at the very right, observed in 2011. The bottom row shows  $J=3-2$  observations of HCO<sup>+</sup> (left) and HCN (right). In all panels the vertical scale is intensity  $T_A^*$  (K) and the horizontal scale is velocity  $V(\text{LSR})$  in km s<sup>-1</sup>.

## 2. Observations

### 2.1. Observing list

We based our selection on the multi-transition <sup>12</sup>CO and <sup>13</sup>CO survey of 126 galaxies by Israel (2020), which originally consisted of the brightest galaxies in the *IRAS* infrared sky survey but was later expanded by adding other galaxies bright in <sup>12</sup>CO. Brightness is an important criterion because the <sup>13</sup>CO line, with its low optical depth, is relatively weak. Because the HCN, HCO<sup>+</sup> and HNC lines are even weaker, the survey presented in this paper is limited to a subset of the brightest galaxies from the CO survey. Because of their greater distance, few infrared-luminous galaxies are bright enough to be included in this limited sample.

Table 2 provides the names of the 46 galaxies observed, their distances, FIR intensities and luminosities, <sup>12</sup>CO(1-0) intensities in the *IRAM* 22'' beam, and overall angular size (Israel 2020 and references therein). The list contains a single ULIRG and five LIRGs. The remainder are lower-luminosity galaxies with a central starburst an AGN, or both.

We made observations in the  $J=1-0$ ,  $J=3-2$  and  $J=4-3$  transitions of HCN, HCO<sup>+</sup> and HNC with the *IRAM* 30m and the *JCMT* 15m telescopes. The  $J=2-1$  transitions are at frequencies with poor atmospheric transmission and observations were not attempted. The  $J=3-2$  transitions were observed with both *IRAM* and *JCMT*, allowing determination of beam-dilution effects. As a byproduct of the early (2008) observations with the *IRAM* ABCD receivers we also obtained CS(3-2) observations

of thirteen galaxies, whereas the later *IRAM* EMIR observations also covered C<sub>2</sub>H(1-0) emission at the band-edge in eleven galaxies.

### 2.2. IRAM 30m observations

We used the *IRAM* 30 m telescope on Pico de Veleta (Granada, Spain)<sup>1</sup> in three observing runs (April 2008, November 2010, and February 2011) in beam-switching mode with a throw of 4'. In the 2008 run, we observed 13 galaxies with the *IRAM* 3-mm and 1.3-mm SIS (ABCD) receivers coupled to 4-MHz back-ends, one line per spectrum. In the 2010 and 2011 runs we used the EMIR receiver to observe both the  $J=1-0$  transitions of HCN, HCO<sup>+</sup>, and HNC, and the  $J=3-2$  transitions of HCN and HCO<sup>+</sup> in single spectra and also reobserved the weaker galaxies from the 2008 run. A sample of the *IRAM* observations is shown in Fig. 1. Individual spectra were reduced with the CLASS package; line parameters were determined by fitting gaussians after baseline subtraction. Intensities were converted to main-beam brightness temperatures using main beam efficiencies  $\eta_{\text{mb}}$  of 0.82 at 89 GHz, 0.74 at 146 GHz, and 0.52 at 255 GHz.

<sup>1</sup> *IRAM* is supported by INSU/CNRS (France), MPG (Germany), and IGN (Spain). The observations enabling the research in this paper have received funding from the European Commission Seventh Framework Programme (FP/2007-2013) under grant agreement No 283393 (RadioNet3)

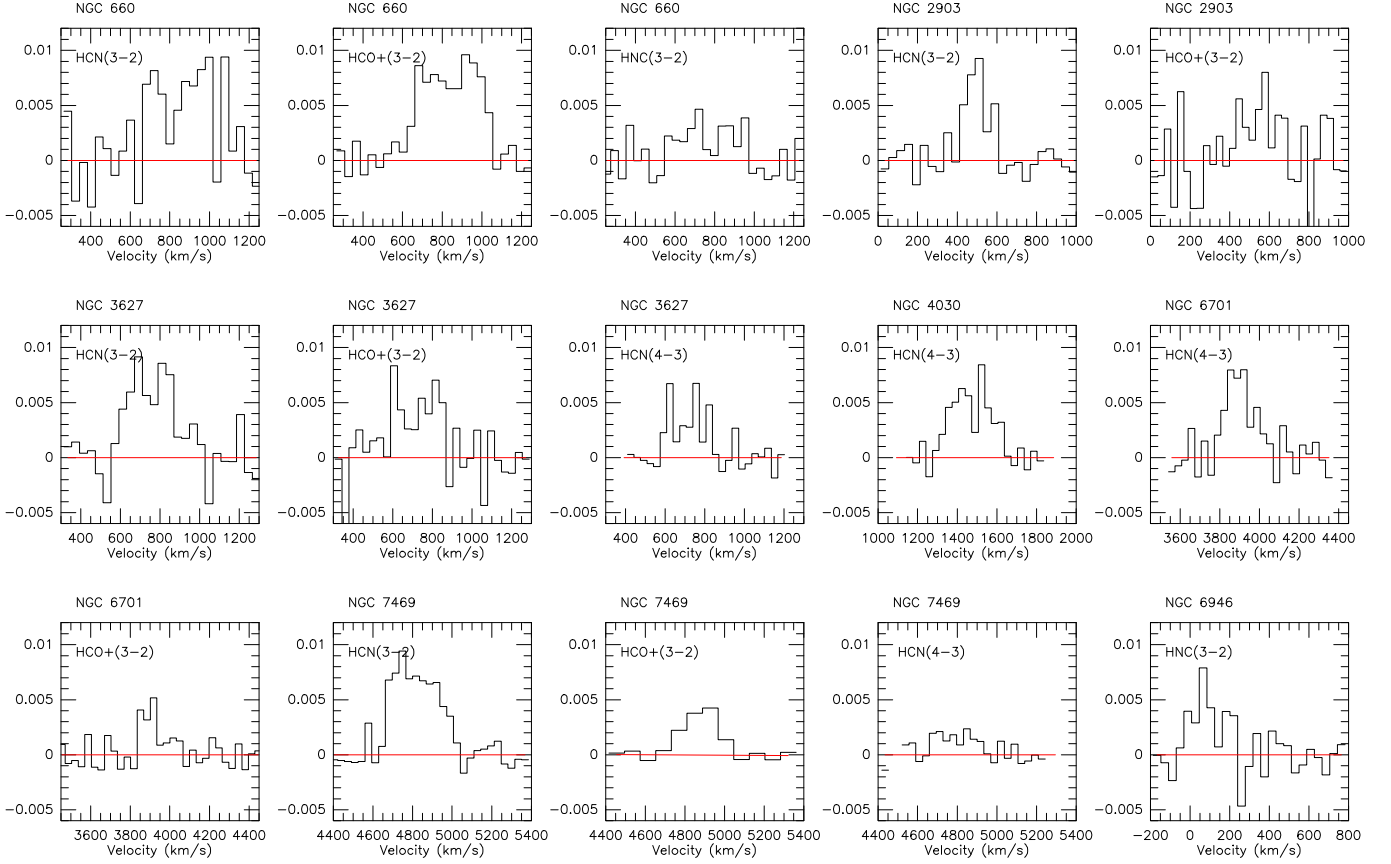


**Fig. 2.** Sample of  $J=3-2$  and  $J=4-3$  molecular line profiles of galaxy centers observed with the 15m *JCMT*. Galaxy and transition are depicted at the top of each panel. In all panels the vertical scale is intensity  $T_A^*$  (K) and the horizontal scale is velocity  $V(\text{LSR})$  in  $\text{km s}^{-1}$ .

### 2.3. *JCMT* 15 m observations

The observations with the 15 m James Clerk Maxwell Telescope (*JCMT*) on Mauna Kea (Hawaii)<sup>2</sup> were obtained at various periods between 2010 and 2013, with a beam-switch throw of  $3'$ , and mostly in queue or backup service mode. The  $J=3-2$  measurements were done with the A3 receiver, and the  $J=4-3$  measurements with the central pixel of the HARP array receiver. We used the FITS protocol to transport the data from SPECX into CLASS. The effectively available band-pass was limited to  $1050 \text{ km s}^{-1}$  in the  $J=3-2$  transition and  $800 \text{ km s}^{-1}$  in the  $J=4-3$  transition. Where weak lines covered much of these ranges, we used the high S/N CO profiles from Israel (2020) as a template to separate the emission from the baseline. We determined integrated intensities by fitting gaussians to the observed profiles after linear baseline subtraction. Because of the limited free baseline, several of the integrated *JCMT* fluxes have larger uncertainties than those determined with the *IRAM* telescope. A sample of the *JCMT* observations is shown in Fig. 2. Antenna temperatures were converted to main-beam brightness temperatures with efficiencies  $\eta_{\text{mb}}(265) = 0.69$  and  $\eta_{\text{mb}}(355) = 0.63$ .

<sup>2</sup> Between 1987 and 2015, the James Clerk Maxwell Telescope (*JCMT*) was operated by the Joint Astronomy Centre on behalf of the Particle Physics and Astronomy Research Council of the United Kingdom, the Netherlands Organization for Scientific Research (until 2013), and the National Research Council of Canada.

## 3. Results

### 3.1. Galaxy sample

The new survey results are listed as velocity-integrated line intensities in Tables 3 and 4. The headers identify molecular species, line transition, telescope used, and the resolution at the observing frequency. Additional *IRAM* and *JCMT* line intensities from the published literature complementing the survey results are included in the tabulation, with the appropriate reference at the bottom.

The database of 46 observed galaxies is further expanded by adding the ground-state HCN,  $\text{HCO}^+$  and HNC intensities of galaxies not included in our observing program, extracted from published *IRAM* 30m surveys. First, we selected from the surveys by Costagliola et al. (2011), Jiang et al. (2011) and Li et al. (2021) an additional 21 galaxies in which the HCN(1-0),  $\text{HCO}^+(1-0)$ , and HNC(1-0) lines were all well-detected, with associated  $^{12}\text{CO}$  and  $^{13}\text{CO}$  data from Li et al. (2015) and Israel (2020). There are no comparable *IRAM* 30m surveys covering the higher transitions.

Secondly, we considered the luminous infrared galaxies specifically targeted in large *IRAM* 30m surveys by Graciá-Carpio et al. 2006, 2008, Graciá-Burillo et al. 2012, Privon et al. 2015, and Herrero-Illana et al. 2019). We found 63 galaxies with well-measured intensities of both HCN(1-0) and  $\text{HCO}^+(1-0)$ , 27 of which are also detected in HNC(1-0) and 10 in HCN(3-2) and  $\text{HCO}^+(3-2)$ . About half of these have corresponding  $^{12}\text{CO}$  and  $^{13}\text{CO}$  data, published by Graciá-Carpio (2009), Li et al. (2015), and Herrero-Illana et al. (2019).

**Table 3.** Galaxy centers: line intensities  $\int(T_{mb}dV)$  (K km s<sup>-1</sup>) for HCN, HCO<sup>+</sup>, HNC

| NGC<br>IC | HCN                    |                        |             |                      | HCO <sup>+</sup>       |                        |             |                      | HNC                    |                       |
|-----------|------------------------|------------------------|-------------|----------------------|------------------------|------------------------|-------------|----------------------|------------------------|-----------------------|
|           | (1-0)                  | (3-2)                  | (3-2)       | (4-3)                | (1-0)                  | (3-2)                  | (3-2)       | (4-3)                | (1-0)                  | (3-2)                 |
|           | <i>IRAM</i>            | <i>IRAM</i>            | <i>JCMT</i> | <i>JCMT</i>          | <i>IRAM</i>            | <i>IRAM</i>            | <i>JCMT</i> | <i>JCMT</i>          | <i>IRAM</i>            | <i>JCMT</i>           |
|           | 27.6"                  | 9.7"                   | 19.0"       | 13.7"                | 27.6"                  | 9.7"                   | 19.0"       | 13.7"                | 27.6"                  | 19.0"                 |
| (1)       | (2)                    | (3)                    | (4)         | (5)                  | (6)                    | (7)                    | (8)         | (9)                  | (10)                   | (11)                  |
| 253       | 68.4±1.4 <sup>a</sup>  | 120±12                 | 77.2±14.2   | 61.1±1.0             | 57.9±1.2 <sup>a</sup>  | 112±25                 | 62.4±1.1    | 66.0±1.0             | 35.5±3.2 <sup>a</sup>  | 34.3±0.7              |
| 470       | 0.75±0.21              | ...                    | ...         | ...                  | ...                    | ...                    | ...         | ...                  | ...                    | ...                   |
| 520       | 2.14±0.14              | ...                    | 1.85±0.41   | ...                  | 3.12±0.13              | ...                    | 2.34±0.27   | ...                  | 1.31±0.12              | ...                   |
| 660       | 6.54±0.65              | 5.34±0.68              | 4.20±0.90   | 2.55±0.50            | 5.13±0.75              | 3.35±0.90              | 4.33±0.29   | ...                  | 2.97±0.31              | 1.74±0.32             |
| 891       | 1.30±0.12              | 1.90±0.55              | 1.66±0.38   | ...                  | 1.33±0.19              | 1.29±0.28              | 1.36±0.35   | ...                  | 0.44±0.08              | ...                   |
| 972       | 1.64±0.18              | ...                    | 1.60±0.55   | ...                  | 1.91±0.17              | ...                    | 0.71±0.35   | ...                  | 0.76±0.17              | ...                   |
| 1055      | 2.35±0.15              | ...                    | 1.55±0.49   | ...                  | 1.40±0.14              | ...                    | 0.44±0.15   | ...                  | 0.79±0.14              | ...                   |
| Maf2      | 15.4±0.5               | 16.6±0.7               | 8.68±0.50   | 3.79±0.79            | 9.48±0.30              | 12.7±1.4               | ...         | 3.48±0.70            | 7.3±0.7 <sup>d</sup>   | 4.04±0.46             |
| 1068      | 25.0±1.2 <sup>b</sup>  | 19.0±1.2 <sup>c</sup>  | 14.3±0.6    | 10.9±0.6             | 14.8±0.8 <sup>b</sup>  | 7.6±0.8 <sup>c</sup>   | 5.43±0.64   | 4.85±0.50            | 9.3±1.2 <sup>b</sup>   | 4.08±0.55             |
| 1084      | 0.71±0.10              | ...                    | 1.85±0.40   | ...                  | 0.62±0.10              | ...                    | 1.26±0.30   | ...                  | 0.28±0.09              | 0.37±0.17             |
| 1097      | 9.31±0.18              | ...                    | 5.99±0.81   | ...                  | 6.67±0.20              | ...                    | 4.52±0.66   | ...                  | 3.06±0.19              | ...                   |
| I342      | 10.8±0.3               | 8.3±0.9                | 3.53±0.35   | 2.7±0.3 <sup>i</sup> | 8.41±0.24              | 7.49±0.94              | 5.05±0.75   | 3.8±0.3 <sup>j</sup> | 4.75±0.11 <sup>j</sup> | 1.47±0.24             |
| 1365      | 14.2±0.7               | 12.0±0.4               | 9.20±0.57   | ...                  | 11.7±1.4               | 9.80±0.36              | ...         | ...                  | 7.24±0.52              | 3.59±0.74             |
| 1808      | 12.5±0.35              | ...                    | ...         | ...                  | 11.7±0.4               | ...                    | ...         | ...                  | 5.12±0.35              | ...                   |
| 2146      | 4.67±0.36              | 4.4±0.3 <sup>c</sup>   | 4.30±0.49   | 4.49±0.89            | 6.70±0.36              | 5.2±0.6 <sup>c</sup>   | ...         | ...                  | 1.86±0.35              | 2.33±0.83             |
| 2559      | 2.96±0.13              | ...                    | 2.52±0.33   | 2.40±0.48            | 3.17±0.18              | ...                    | ...         | ...                  | 1.03±0.13              | 0.14±0.13             |
| 2623      | 1.77±0.38              | 2.07±0.76              | 1.82±0.34   | 1.29±0.39            | 1.87±0.25              | 3.18±0.48              | ...         | ...                  | ...                    | 1.83±0.2 <sup>f</sup> |
| 2903      | 3.35±0.12              | ...                    | 1.88±0.19   | 1.36±0.23            | 1.81±0.32              | ...                    | 1.62±0.32   | ...                  | 1.23±0.12              | 0.61±0.48             |
| 3034      | 29±3 <sup>c</sup>      | 27±3 <sup>c</sup>      | 13.4±0.7    | 7.51±0.55            | 40.2±2.5 <sup>c</sup>  | 34.0±2.0 <sup>c</sup>  | 27.2±1.1    | 19.3±1.9             | 12±1.5 <sup>e</sup>    | 3.58±1.52             |
| 3079      | 7.57±0.58              | 15.8±1.5               | 6.91±0.46   | 3.44±0.47            | 6.54±0.23              | 16.2±1.8               | 6.14±1.05   | 3.78±0.49            | 2.2±0.14 <sup>j</sup>  | 3.1±1.2               |
| 3310      | 0.30±0.08              | ...                    | 1.41±0.72   | ...                  | 0.67±0.40              | ...                    | 0.74±0.28   | ...                  | 0.32±0.12              | ...                   |
| 3627      | 2.79±0.14              | ...                    | 2.23±0.40   | 1.64±0.16            | 2.93±0.15              | 2.1±0.2 <sup>j</sup>   | ...         | ...                  | 0.78±0.19              | 0.58±0.20             |
| 3628      | 5.35±0.36              | 3.25±0.73              | 3.42±0.20   | 2.01±0.17            | 5.60±0.23              | 4.67±0.93              | ...         | ...                  | 3.4±0.3 <sup>d</sup>   | ...                   |
| 3690      | 2.51±0.30              | 1.58±0.38 <sup>g</sup> | 0.99±0.21   | 0.44±0.19            | 3.62±0.18              | 4.72±0.44 <sup>g</sup> | ...         | ...                  | 0.90±0.19              | ...                   |
| 4030      | 3.45±0.14              | 2.00±0.50              | 1.37±0.45   | 1.57±0.17            | 1.76±0.17              | 0.90±0.26              | ...         | ...                  | 1.80±0.17              | ...                   |
| 4038      | 2.57±0.10              | 0.91±0.19              | 0.95±0.21   | 1.10±0.71            | 3.53±0.10              | 1.53±0.33              | 1.44±0.28   | ...                  | 1.13±0.07              | ...                   |
| 4102      | 3.75±0.32              | 3.64±0.68              | 2.01±0.62   | ...                  | 2.28±0.51              | 2.02±0.61              | ...         | 2.74±0.17            | 2.81±0.23              | ...                   |
| 4321      | 4.93±0.28              | 3.09±0.26              | 2.23±0.60   | 1.75±0.46            | 3.19±0.12              | 2.12±0.39              | ...         | ...                  | 1.64±0.08              | ...                   |
| 4414      | 3.76±0.39              | ...                    | 1.05±0.39   | 0.92±0.17            | 2.68±0.30              | 1.34±0.41              | ...         | ...                  | 1.03±0.15              | ...                   |
| 4527      | 3.41±0.24              | 1.90±0.21              | 1.33±0.44   | ...                  | 3.07±0.23              | 1.87±0.20              | ...         | ...                  | 1.54±0.28              | ...                   |
| 4569      | 3.21±0.15              | 2.35±0.38              | 0.76±0.23   | 0.69±0.25            | 2.50±0.14              | 2.08±0.33              | ...         | ...                  | 0.73±0.15              | ...                   |
| 4666      | 2.19±0.07              | 1.82±0.46              | 0.60±0.38   | 1.36±0.11            | 1.42±0.10              | 0.63±0.24              | ...         | ...                  | 1.36±0.14              | ...                   |
| 4826      | 7.19±0.39              | 1.77±0.36              | 1.94±0.70   | 1.22±0.32            | 4.46±0.10              | 1.33±0.21              | ...         | ...                  | 3.03±0.15              | 1.32±0.31             |
| 5033      | 1.28±0.13              | ...                    | 1.26±0.51   | ...                  | 0.95±0.15              | ...                    | 0.62±0.26   | ...                  | 1.07±0.17              | ...                   |
| 5055      | 2.59±0.44              | 1.85±0.48              | 0.90±0.60   | 0.61±0.22            | 1.43±0.28              | ...                    | ...         | ...                  | 0.71±0.15              | ...                   |
| 5194      | 7.15±0.29              | 2.31±0.24              | 1.38±0.70   | 1.36±0.43            | 3.36±0.15              | 1.43±0.29              | ...         | ...                  | 2.74±0.14              | 0.48±0.29             |
| 5236      | 8.54±0.26              | ...                    | 3.86±0.30   | 1.76±0.20            | 10.4±0.4               | ...                    | ...         | 2.52±0.36            | 4.3±0.3 <sup>d</sup>   | 1.30±0.28             |
| 5775      | 1.39±0.36              | 0.85±0.19              | ...         | *                    | 1.30±0.39              | 0.46±0.31              | ...         | ...                  | 0.27±0.17              | ...                   |
| 6240      | 3.80±0.20              | 7.8±0.31 <sup>h</sup>  | 4.70±0.29   | 4.61±1.42            | 6.37±0.20              | 7.1±1.9 <sup>h</sup>   | 1.79±1.15   | ...                  | 0.78±0.15              | ...                   |
| 6701      | 2.32±0.06              | 2.55±0.25              | 1.09±0.20   | 1.85±0.46            | 2.37±0.07              | 2.41±0.24              | 3.43±0.75   | ...                  | 0.96±0.09              | 0.50±0.50             |
| 6946      | 9.9±0.1 <sup>c</sup>   | 9.2±0.6 <sup>c</sup>   | 3.85±0.36   | 1.53±0.22            | 8.5±0.1 <sup>c</sup>   | 8.6±0.6 <sup>c</sup>   | 3.19±0.38   | ...                  | 4.0±0.4 <sup>d</sup>   | 1.98±0.54             |
| 6951      | 2.68±0.13              | 1.99±0.38              | 1.13±0.39   | ...                  | 1.95±0.08              | 2.24±0.41              | 1.30±0.44   | ...                  | 1.50±0.09              | 0.67±0.20             |
| 7469      | 2.56±0.13              | 2.76±0.34 <sup>g</sup> | 2.01±0.51   | 0.73±0.25            | 2.68±0.12              | 2.08±0.42 <sup>g</sup> | 1.51±0.19   | ...                  | 1.32±0.13              | 1.09±0.44             |
| 7714      | 0.56±0.18              | ...                    | ...         | ...                  | 0.18±0.17              | ...                    | ...         | ...                  | ...                    | ...                   |
| 7771      | 5.35±0.60              | 3.33±0.58 <sup>g</sup> | 1.19±0.23   | ...                  | 5.59±0.26              | 1.98±0.37 <sup>g</sup> | 2.48±0.56   | ...                  | 2.31±0.15              | 1.21±0.43             |
| A220      | 8.16±0.17 <sup>g</sup> | 18.0±0.5 <sup>g</sup>  | 12.5±0.6    | 3.89±0.59            | 3.77±0.21 <sup>g</sup> | 4.57±0.23 <sup>g</sup> | ...         | 2.96±0.49            | 7.8±0.8 <sup>g</sup>   | ...                   |

References to intensities taken from the literature: a. Aladro et al. (2015); b. Average from Krips et al. (2008), Costagliola et al. (2011), and Aladro et al. (2015); c. Krips et al. (2008); d. Hüttemeister et al. (1995); e. Average from Hüttemeister et al. (1995) and Aladro et al. (2015); f. Pérez-Beaupuits et al. (2007); g. Graciá-Carpio et al. 2008; h. Li et al. (2018); i. Tan et al. (2018); j. Li et al. (2021)

In total, there are well-established intensities of the three  $J=1-0$  HCN, HCO<sup>+</sup> and HNC lines for 94 galaxies covering a large luminosity range ( $9.2 \leq \log L_{FIR} \leq 12.3$ ). An additional 36 galaxies have good HCN(1-0) and HCO<sup>+</sup>(1-0) line intensities only. About 50 galaxies have good HCN(3-2) and HCO<sup>+</sup>(3-2) data, mostly provided by our new survey that also

contributes a smaller number of additional HNC(3-2), HCN(4-3) and HCO<sup>+</sup>(4-3) data.

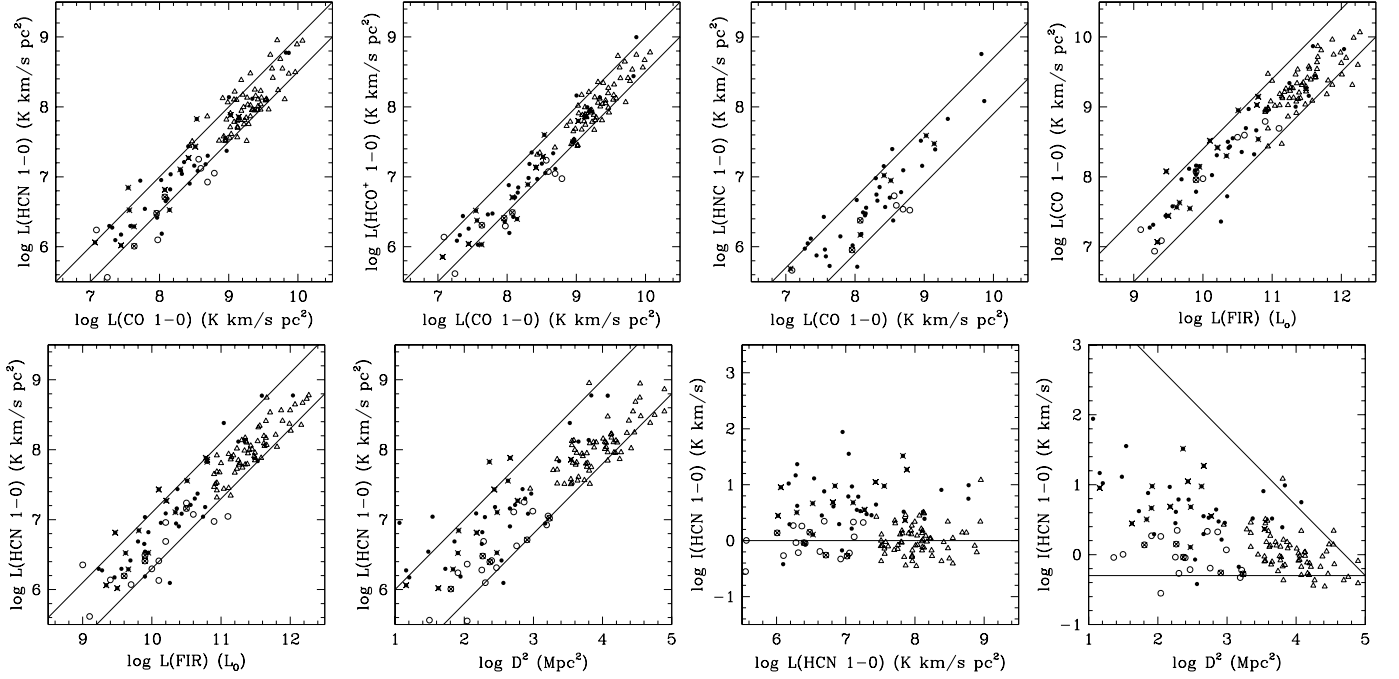


**Fig. 3.** Top row: galaxy center luminosity-luminosity relations in identical 22'' beams. Leftmost panels:  $J=1-0$  HCN and  $\text{HCO}^+$  versus  $^{12}\text{CO}$  with constant ratios 0.10 and 0.03 marked by solid lines. Rightmost panels: HNC(1-0) versus  $^{12}\text{CO}$  with constant ratios 0.050 and 0.008, and central  $^{12}\text{CO}$  versus global far-infrared (FIR) continuum with constant ratios  $2.5 \times 10^{-2}$  and  $3.2 \times 10^{-3} \text{ K km/s pc}^2/L_0$  marked. Bottom row, leftmost panel: central HCN(1-0) versus global FIR continuum with constant ratios of  $2 \times 10^{-3}$  and  $1.25 \times 10^{-4}$  marked, very similar to the HCN/CO (top left) and HCN/FIR (top right) diagrams. Center left panel: relation between HCN luminosity ( $L(\text{HCN}) \propto I(\text{HCN}) \times D^2$ ) and distance ( $D^2$ ). Center right panel: relation between luminosity  $L(\text{HCN})$  and intensity  $I(\text{HCN})$ ; vertical line marks constant surface brightness of 1 K km/s. Rightmost panel: relation between  $I(\text{HCN})$  and distance ( $D^2$ ), with a horizontal line of resolved surface brightness of 0.5 K km/s and a diagonal line of unresolved point-like emission (cf. Table 1). In these and following diagrams, filled circles denote the new data from this paper, open circles literature data on similar galaxies, crosses galaxies with an identified AGN and triangles literature survey data on (U)LIRGs.

The results of least-squares regression fits, of the form  $\log(y) = a \log(x) + b$ , to the data in this figure and the following figures are given in Table 8.

### 3.2. Normalized intensities

Because the  $J=1-0$  line frequencies of HCN, HNC and  $\text{HCO}^+$  are very close together, their intensities measured with the IRAM 30m telescope are directly comparable. This not true, however, for measurements in other transitions, for measurements with a different telescope aperture, and for measurements of species such as CO, which are all observed at a different spatial resolution. Molecular line intensities observed at different resolutions must be reduced (normalized) to the same resolution before they can be compared in a meaningful way. The resolution of 22'' is conveniently intermediate between the resolutions of the IRAM  $J=1-0$  (27'') and JCMT  $J=3-2$  (19'') lines, and it is also the reference for the CO transition ladders published by Israel (2020). Only minor extrapolations are required to bring the observed  $J=1-0$  and  $J=3-2$  intensities to values corresponding to this resolution.

For  $J=1-0$  HCN we used the intensities of 36 sample galaxies measured in larger beams (NRAO  $\theta = 72''$ , 25 galaxies; SEST  $\theta = 57''$ , 14 galaxies; FCRAO  $\theta = 50''$ , 6 galaxies; OSO  $\theta = 44''$ , 4 galaxies) in combination with the IRAM measurements ( $\theta = 27.6''$ ) of the present survey to extrapolate the latter to the equivalent flux at 22''. On average, the extrapolation is almost linear with the resolution, intermediate between

the extremes expected for infinitely large (extended) and infinitely small (pointlike) sources. The average extrapolation factor  $f_{10} = 1.2$  (corresponding to a power law extrapolation with index 0.8) was used for the remaining galaxies lacking observations at other resolutions. As the modest change of resolution limits possible multiplication factors to  $1.00 \leq f_{10} \leq 1.57$ , extrapolation uncertainties add relatively little to the overall errors.

We applied the HCN(1-0) normalization factors to the  $\text{HCO}^+(1-0)$  and HNC(1-0) intensities because these species have, unlike HCN, few observations at other resolutions. The implicit assumption of identical spatial emission distributions likewise does not introduce more than small errors.

The paucity of published HCN,  $\text{HCO}^+$ , or HNC measurements in higher transitions at other resolutions than presented here was the rationale for observing  $J=3-2$  HCN and  $\text{HCO}^+$  transitions with both the JCMT 15m and IRAM 30m facilities. Their resolutions differ by a factor of two (9.6'' and 19''), from which the normalized intensity at 22'' is once again derived by a modest extrapolation, with correction factors limited to  $1.00 \geq f_{32} \geq 0.75$ . The actual average reduction factors derived from the data in Table 3 are  $f_{\text{HCN}32} = 0.91$  (33 galaxies) and  $f_{\text{HCO}32} = 0.94$  (14 galaxies). The difference is not significant and justifies the assumption of very similar HCN and  $\text{HCO}^+$  emission distributions. No duplicate  $J3-2$  data were obtained for

**Table 4.** Galaxy centers: CS, C<sub>2</sub>H line intensities  $\int(T_{mb}dV)$ 

| NGC<br>IC | CS(3-2)<br>16.8''<br>K km s <sup>-1</sup> | C <sub>2</sub> H(1-0)<br>27.6''<br>K km s <sup>-1</sup> |
|-----------|---|---|
| (1)       | (2)                                       | (3)   |
| N 253     | ...                                       | 34.64±0.45 <sup>a</sup>                                 |
| N 660     | 1.70±0.22                                 | 2.77±0.28   |
| N 891     | 0.41±0.07                                 | 0.57±0.24   |
| Maff2     | 4.41±0.41                                 | ...   |
| N1055     | 0.40±0.14                                 | ...   |
| N1068     | ...                                       | 8.84±2.20 <sup>ab</sup>                                 |
| N1365     | 2.80±0.35                                 | ...   |
| ..I342    | 4.03±0.20                                 | ...   |
| N1808     | ...                                       | 5.43±1.09   |
| N2146     | 1.22±0.23 <sup>c</sup>                    | 3.85±0.79   |
| N2623     | 0.90±0.11                                 | ...   |
| N2903     | 0.58±0.08                                 | ...   |
| N3034     | 12.1±0.5 <sup>c</sup>                     | 20.61±0.23 <sup>a</sup>                                 |
| N3079     | 4.98±0.29                                 | 2.90±0.30 <sup>bd</sup>                                 |
| N3628     | 3.77±0.23                                 | ...   |
| N3690     | 0.68±0.09 <sup>c</sup>                    | 1.20±0.18 <sup>e</sup>                                  |
| N4102     | 1.09±0.20                                 | ...   |
| N5055     | 2.89±0.42                                 | ...   |
| N5194     | 1.27±0.07 <sup>c</sup>                    | 1.26±0.07 <sup>a</sup>                                  |
| N5236     | 3.36±0.22                                 | 4.01±0.08 <sup>a</sup>                                  |
| N5775     | 0.27±0.13 <sup>c</sup>                    | 1.90±0.70   |
| N6240     | 0.60±0.04 <sup>c</sup>                    | 1.19±0.20 <sup>be</sup>                                 |
| N7469     | ...                                       | 1.71±0.29 <sup>ab</sup>                                 |
| N7771     | ...                                       | 1.10±0.18 <sup>b</sup>                                  |

References to measurements from the literature: a. Aladro et al. (2015); b. Costagliola et al. (2011); d. Li et al. (2019); e. Jiang et al. (2011).

the HNC lines but the spatial distributions of HNC and HCN are even more likely to be identical so that the same factors apply. Finally, we assumed the resolution dependence of the  $J=4-3$  HCN and HCO<sup>+</sup> intensities to be the same as that of the  $J=3-2$  lines and interpolated the latter to obtain the normalization factors for the  $J=4-3$  intensities, with resulting averages  $f_{\text{HCN}43} = 0.65$  (24 galaxies) and  $f_{\text{HCO}4-3} = 0.74$  (8 galaxies). In Table 5 all intensities are normalized to resolutions of 22'' by the appropriate factors. This table also includes *IRAM*  $J=2-1$  HCN intensities (14'') from Krips et al. 2008.

### 3.3. Line ratios and transition ladders

In columns 2 through 7 of Table 6, intensities of HCO<sup>+</sup> and HNC relative to HCN are listed. The resolutions change with each transition, but they are near-identical for lines observed in the same transition. The *IRAM* HCO<sup>+</sup>/HCN and HNC/HCN intensity ratios are each determined from lines in the same spectrum and are thus quite accurate. The JCMT-derived line ratios are less accurate as they are determined from separate single-line *JCMT* observations made on different occasions. The HCN/CO intensity ratios in Column 8 are based on the normalized  $J=1-0$  HCN intensities from Table 5 and the  $J=1-0$  CO intensities from Israel(2020) and refer to identical beams of 22''. The transition ladder ratios of HCN, HNC and HCO<sup>+</sup> in columns 9 through 14 are likewise derived from the normalized values in Table 5.

## 4. Analysis

This section identifies what observational patterns exist for the various galaxies and in particular which luminosities and luminosity ratios, if any, show a degree of correlation. Possible explanations for the resulting findings and their meaning are discussed in the following Section 5.

The *IRAM*30m line measurements of both HCN(1-0) and HCO<sup>+</sup>(1-0) in 130 galaxies constitute a sample with a size and homogeneity that renders it highly suitable to the large-scale investigation of the molecular gas in galaxies of a diverse nature and wide range of luminosities. Such investigations have been carried out before, first by Gao & Solomon (2004b), by Baan et al. (2008), and most recently by Li et al. (2021) but there are major differences between their surveys and ours. The Gao & Solomon data set is half the size, has a poorer resolution (*NRAO* 12m versus *IRAM* 30m), contains only ground-state HCN and CO transitions, but attempts to cover entire galaxies instead of just central regions. The data set used by Baan et al. covers the HCN, HCO<sup>+</sup> and HNC ground state only, but includes CN and CS lines, it is smaller, less complete, and combines data from telescopes with different and generally larger beams making it very inhomogeneous and less accurate. The Li et al. *IRAM* 30m data set contains a similar number of detected galaxies (124 versus 130 with both HCN and HCO<sup>+</sup>, and 85 versus 94 with also HNC) but it also includes only ground state transitions.

In the following, molecular line luminosities<sup>3</sup> and intensities all refer to the normalized (22'') central aperture discussed above. The far-infrared intensities and luminosities, however, refer to the *IRAS* aperture which is a factor of 100 greater and should be considered more representative for the galaxy as a whole.

### 4.1. HCN(1-0) and HCO<sup>+</sup>(1-0) versus FIR and CO(1-0) luminosities

Comparison shows that the normalized central HCN(1-0), HCO<sup>+</sup>(1-0), and HNC(1-0) luminosities are all linearly correlated with each other, as well as the CO luminosity, with slopes corresponding to average ratios HCN/CO = 0.046, HCO<sup>+</sup>/CO = 0.041, and HNC/CO = 0.021 (Fig 3). In each relation, the dispersion does not change with luminosity. It exceeds the observational uncertainty and reflects variation between individual galaxies. Solomon et al. (1992) were the first to draw attention to the tight relation between global HCN and FIR luminosities, further elaborated by Gao & Solomon (2004a), and rediscovered or confirmed by almost all later authors for HCN(1-0), HCO<sup>+</sup>(1-0), HNC(1-0), CS(3-2), and far-infrared luminosity in matched beams.

The CO line and FIR continuum luminosities are also linearly related (rightmost panel of Fig. 3) and it makes little difference whether the other luminosities are plotted as a function of CO or of FIR luminosity. This is illustrated by the similarity of the CO-FIR, HCN-CO and HCN-FIR diagrams in Fig. 3 (top right, top left and bottom left panels).

In the bottom row of Fig. 3 we further investigate the relations between the derived luminosity  $L$ , the observed surface brightness  $I$ , and the assumed distance  $D$ . Measured in the same normalized beam, luminosities vary with surface brightness and distance ( $L \propto I \times D^2$ ) only. The luminosity  $L(\text{HCN})$  is strongly correlated with distance  $D^2$  (center left panel) and very weakly

<sup>3</sup> Throughout this paper, line luminosities are defined as the product of line flux in K km/s and beam surface area in pc<sup>2</sup>

**Table 5.** Galaxy centers: molecular line intensities  $\int(T_{mb}dV)$  (K km s<sup>-1</sup>) normalized to 22'' beams (see text)

| NGC<br>(1) | HCN          |                           |              |              | HNC          |              | HCO <sup>+</sup> |              |               |
|------------|--------------|---------------------------|--------------|--------------|--------------|--------------|------------------|--------------|---------------|
|            | (1-0)<br>(2) | (2-1) <sup>a</sup><br>(3) | (3-2)<br>(4) | (4-3)<br>(5) | (1-0)<br>(6) | (3-2)<br>(7) | (1-0)<br>(8)     | (3-2)<br>(9) | (4-3)<br>(10) |
| N0253      | 87.60        | ...                       | 70.12        | 44.78        | 45.44        | 31.15        | 74.11            | 54.93        | 43.71         |
| N0520      | 2.85         | ...                       | 1.7          | ...          | 1.74         | ...          | 4.15             | 2.20         | ...           |
| N0660      | 9.29         | 6.4                       | 3.99         | 2.15         | 4.22         | 1.35         | 7.29             | 4.58         | ...           |
| N0891      | 1.96         | ...                       | 1.61         | ...          | 0.66         | ...          | 2.01             | 1.4          | ...           |
| N0972      | 1.97         | ...                       | 1.5          | ...          | 0.9          | ...          | 2.29             | 0.5          | ...           |
| N1055      | 2.82         | ...                       | 1.4          | ...          | 0.95         | ...          | 1.68             | 0.4          | ...           |
| MAF2       | 23.25        | 12.0                      | 7.54         | 2.40         | 11.02        | 3.51         | 14.31            | 6.10         | 2.19          |
| N1068      | 32.75        | 14.9                      | 13.44        | 8.92         | 12.18        | 3.84         | 19.39            | 5.05         | 3.85          |
| N1084      | 0.85         | ...                       | 1.7          | ...          | 0.3          | ...          | 0.74             | 1.2          | ...           |
| N1097      | 11.17        | ...                       | 5.50         | ...          | 3.67         | ...          | 8.00             | 4.20         | ...           |
| IC342      | 14.69        | ...                       | 2.93         | 1.48         | 6.46         | 1.22         | 11.44            | 4.60         | 2.88          |
| N1365      | 18.60        | ...                       | 8.68         | ...          | 9.48         | 3.39         | 15.33            | 7.40         | ...           |
| N2146      | 6.12         | 4.3                       | 4.28         | 4.42         | 2.44         | 2.32         | 8.78             | 4.70         | ...           |
| N2559      | 3.55         | ...                       | 2.30         | ...          | 1.24         | ...          | 3.80             | ...          | ...           |
| N2623      | 2.46         | ...                       | 1.77         | 1.2          | ...          | 1.78         | 2.60             | 4.00         | ...           |
| N2903      | 4.19         | ...                       | 1.70         | ...          | 1.54         | ...          | 2.26             | 1.50         | ...           |
| N3034      | 35.67        | 14.2                      | 11.50        | 4.58         | 14.76        | 3.1          | 49.45            | 25.90        | 16.49         |
| N3079      | 9.46         | ...                       | 5.77         | 1.92         | 2.7          | 2.6          | 8.18             | 4.97         | 1.91          |
| N3310      | 0.38         | ...                       | 1.3          | ...          | 0.4          | ...          | 0.84             | 0.7          | ...           |
| N3627      | 2.79         | ...                       | 1.90         | ...          | 0.8          | 0.5          | 2.93             | ...          | ...           |
| N3628      | 7.60         | ...                       | 3.46         | 2.08         | 4.83         | ...          | 7.95             | 4.9          | ...           |
| N3690      | 3.29         | ...                       | 0.89         | 0.3          | 1.18         | ...          | 4.74             | 3.00         | ...           |
| N4030      | 4.42         | ...                       | 1.26         | 1.20         | 2.30         | ...          | 2.25             | 0.6          | ...           |
| N4038      | 3.37         | ...                       | 0.96         | 1.1          | 1.48         | ...          | 4.62             | 1.42         | ...           |
| N4102      | 4.80         | ...                       | 1.77         | ...          | 3.60         | ...          | 2.92             | 1.1          | ...           |
| N4321      | 6.16         | ...                       | 2.08         | 1.4          | 2.05         | ...          | 3.99             | 1.5          | 1.7           |
| N4414      | 4.63         | ...                       | 1.0          | ...          | 1.27         | ...          | 3.30             | ...          | ...           |
| N4527      | 4.09         | ...                       | 1.23         | ...          | 1.85         | ...          | 3.68             | 1.30         | ...           |
| N4569      | 4.85         | 1.0                       | 0.59         | 0.3          | 1.10         | ...          | 3.78             | 0.70         | ...           |
| N4666      | 2.98         | ...                       | 0.47         | 0.62         | 1.85         | ...          | 1.93             | 0.2          | ...           |
| N4826      | 8.99         | 2.5                       | 1.98         | 1.3          | 3.79         | 1.3          | 5.58             | 0.7          | ...           |
| N5033      | 1.28         | ...                       | 1.2          | ...          | 1.07         | ...          | 0.95             | 1.90         | ...           |
| N5055      | 3.19         | ...                       | 0.77         | 0.4          | 0.9          | ...          | 1.76             | ...          | ...           |
| N5194      | 9.51         | 1.4                       | 1.23         | 1.0          | 3.64         | 0.4          | 4.47             | 0.90         | ...           |
| N5236      | 10.50        | ...                       | 3.50         | ...          | 5.29         | ...          | 12.79            | ...          | 2.52          |
| N5775      | 1.64         | ...                       | ...          | ...          | 0.3          | 1.3          | 1.53             | ...          | ...           |
| N6240      | 5.62         | 5.6                       | 4.21         | 3.2          | 1.15         | ...          | 9.43             | 5.25         | ...           |
| N6701      | 2.32         | ...                       | 0.91         | 1.0          | 0.96         | ...          | 2.37             | 3.70         | ...           |
| N6946      | 12.97        | 5.3                       | 3.18         | 0.83         | 5.24         | 1.6          | 11.13            | 2.57         | ...           |
| N6951      | 3.56         | 3.1                       | 1.00         | ...          | 2.00         | 0.6          | 2.59             | 1.16         | ...           |
| N7469      | 3.28         | ...                       | 1.88         | 0.6          | 1.69         | 1.0          | 3.43             | 1.41         | ...           |
| N7771      | 8.08         | ...                       | 0.95         | ...          | 3.49         | 1.0          | 8.44             | 2.61         | ...           |
| A220       | 9.79         | ...                       | 11.54        | 3.01         | 9.36         | ...          | 4.52             | 3.20         | ...           |

Note: <sup>a</sup> Based on IRAM measurements by Krips et al. (2008)

or not at all with observed intensity  $I(\text{HCN})$  (center right panel). Thus, the luminosities are essentially determined by the distance and not by the intensity of the observed galaxies. The intensity  $I(\text{HCN})$  and distance  $D^2$  are weakly anti-correlated (right-most panel). The surface brightness goes down with increasing distance as the constant aperture covers an increasingly larger part of the galaxy. As Gao & Solomon (2004b) already surmised, the HCN surface brightness peaks at the nucleus and drops when it is averaged over increasingly larger surface area. This is well-illustrated by HCN line maps (Green et al. 2016, Tan et al. 2018, Jiménez-Donaire et al. 2019) that include several of the galaxies in our sample. Because of the anticorrelation between  $I(\text{HCN})$  and  $D^2$ , the relation between luminosity  $L(\text{HCN})$  and distance  $D^2$  is modestly sub-linear. The smaller departure from linearity, and the larger dispersion in the  $L(\text{CO})$ -

$L(\text{FIR})$  and  $L(\text{HCN})$ - $L(\text{FIR})$  diagrams is due to the aperture mismatch between the FIR continuum and the molecular line measurements. In matched apertures, the discrepancy disappears (Li et al. 2021). Nevertheless, comparison of the results by Gao & Solomon (2004b) and Li et al. (2021) shows that the use of global instead of central luminosities leads to similar results.

As long as the derived luminosities are dominated by the distance factor  $D^2$  and no large changes occur in the underlying line intensities, the luminosity plots will show (almost) linear relationships. As we will show, the line intensities in this paper tend to be characterized by constant ratios. The observed linearity of luminosity-versus-luminosity plots thus reflects geometric factors unrelated to intrinsic galaxy properties.



**Table 6.** Galaxy centers: molecular line ratios

| NGC              | HCO <sup>+</sup> /HCN |                  |       |        |                    | HNC/HCN |       | HCN/CO  | HCN                  |         |         | HNC     | HCO <sup>+</sup> |         |
|------------------|-----------------------|------------------|-------|--------|--------------------|---------|-------|---------|----------------------|---------|---------|---------|------------------|---------|
|                  | 1-0                   | 2-1 <sup>a</sup> | 3-2   | 3-2    | 4-3                | 1-0     | 3-2   | 1-0/1-0 | 2-1/1-0 <sup>b</sup> | 3-2/1-0 | 4-3/1-0 | 3-2/1-0 | 3-2/1-0          | 4-3/1-0 |
|                  | 27.6''                | 34.7''           | 9.7'' | 19.0'' | 13.7''             | 27.6''  | 19''  | 22''    | 22''                 | 22''    | 22''    | 22''    | 22''             | 22''    |
| (1)              | (2)                   | (3)              | (4)   | (5)    | (6)                | (7)     | (8)   | (9)     | (10)                 | (11)    | (12)    | (13)    | (14)             | 15      |
| 253              | 0.85                  | ...              | 0.93  | 0.81   | 1.21 <sup>c</sup>  | 0.52    | 0.45  | 0.085   | ...                  | 0.80    | 0.51    | 0.69    | 0.74             | 0.59    |
| 520              | 1.46                  | ...              | ...   | 1.27   | ...                | 0.61    | ...   | 0.025   | ...                  | 0.60    | 0.53    | ...     | ...              | ...     |
| 660              | 0.78                  | ...              | 0.63  | 1.03   | 1.04 <sup>d</sup>  | 0.45    | 0.34  | 0.060   | 0.69                 | 0.43    | 0.23    | 0.32    | 0.63             | ...     |
| 891              | 1.02                  | ...              | 0.68  | 0.82   | ...                | 0.34    | ...   | 0.014   | ...                  | 0.82    | ...     | ...     | 0.69             | ...     |
| 972              | 1.17                  | ...              | ...   | 0.4:   | ...                | 0.46    | ...   | 0.029   | ...                  | 0.76    | ...     | ...     | 0.18             | ...     |
| 1055             | 0.60                  | ...              | ...   | 0.3:   | ...                | 0.34    | ...   | 0.037   | ...                  | 0.50    | ...     | ...     | 0.24             | ...     |
| Maf2             | 0.62                  | ...              | 0.77  | ...    | 0.92               | 0.47    | 0.47  | 0.106   | 0.52                 | 0.32    | 0.10    | 0.32    | 0.43             | ...     |
| 1068 *           | 0.59                  | 0.74             | 0.40  | 0.38   | 0.46 <sup>cd</sup> | 0.40    | 0.29  | 0.195   | 0.46                 | 0.41    | 0.27    | 0.32    | 0.26             | 0.20    |
| 1084             | 0.87                  | ...              | ...   | 0.68   | ...                | 0.39    | 0.2:  | 0.028   | ...                  | ...     | ...     | ...     | ...              | ...     |
| 1097 *           | 0.72                  | ...              | ...   | 0.75   | ...                | 0.33    | ...   | 0.082   | ...                  | 0.49    | ...     | ...     | 0.53             | ...     |
| I342             | 0.78                  | ...              | 0.90  | 1.43   | 1.41 <sup>c</sup>  | 0.59    | 0.42  | 0.091   | 0.20                 | 0.10    | 0.40    | 0.14    | 0.25             | ...     |
| 1365 *           | 0.82                  | 0.74             | 0.81  | ...    | 1.11 <sup>cd</sup> | 0.51    | 0.39  | 0.072   | ...                  | 0.47    | ...     | 0.36    | 0.48             | ...     |
| 1808 *           | 0.94                  | 1.04             | ...   | ...    | 0.96 <sup>cd</sup> | 0.41    | ...   | ...     | ...                  | ...     | ...     | ...     | ...              | ...     |
| 2146             | 1.44                  | ...              | 1.18  | ...    | ...                | 0.40    | 0.5:  | 0.033   | 0.70                 | 0.70    | 0.72    | ...     | 0.54             | ...     |
| 2559             | 1.07                  | ...              | ...   | ...    | ...                | 0.35    | ...   | 0.046   | ...                  | 0.65    | ...     | ...     | ...              | ...     |
| 2623             | 1.06                  | ...              | 1.54  | ...    | ...                | ...     | 0.99  | 0.137   | ...                  | 0.72    | 0.48    | ...     | 1.5              | ...     |
| 2903             | 0.54                  | ...              | ...   | 0.86   | ...                | 0.37    | ...   | 0.052   | ...                  | 0.41    | ...     | ...     | 0.66             | ...     |
| 3034             | 1.39                  | ...              | 1.26  | 2.03   | 2.72 <sup>c</sup>  | 0.41    | 0.27  | 0.052   | 0.40                 | 0.32    | 0.13    | 0.21    | 0.52             | 0.33    |
| 3079 *           | 0.86                  | ...              | 1.03  | 0.89   | 1.10               | 0.91    | 0.2:  | 0.040   | ...                  | 0.61    | 0.20    | ...     | 0.61             | 0.23    |
| 3627 *           | 1.05                  | ...              | ...   | ...    | 0.88 <sup>d</sup>  | 0.28    | 0.3:  | 0.038   | ...                  | 0.68    | ...     | ...     | ...              | ...     |
| 3628             | 1.05                  | 1.34             | 1.44  | ...    | 2.78 <sup>d</sup>  | 0.64    | ...   | 0.037   | ...                  | 0.46    | 0.27    | ...     | 0.62             | ...     |
| 3690             | 1.44                  | ...              | 2.99  | ...    | ...                | 0.36    | ...   | 0.048   | ...                  | 0.27    | 0.10    | ...     | 0.63             | ...     |
| 4030             | 0.51                  | ...              | 0.45  | ...    | ...                | 0.53    | ...   | 0.105   | ...                  | 0.29    | 0.27    | ...     | 0.27             | ...     |
| 4038             | 1.37                  | ...              | 1.68  | 1.52   | ...                | 0.44    | ...   | 0.072   | ...                  | 0.29    | 0.34    | ...     | 0.31             | ...     |
| 4102 *           | 0.61                  | ...              | 0.55  | ...    | ...                | 0.75    | ...   | 0.064   | ...                  | 0.37    | ...     | ...     | 0.38             | ...     |
| 4321             | 0.65                  | ...              | 0.69  | ...    | ...                | 0.33    | ...   | 0.075   | ...                  | 0.34    | 0.23    | ...     | 0.38             | ...     |
| 4414 *           | 0.71                  | ...              | ...   | ...    | ...                | 0.27    | ...   | 0.091   | ...                  | 0.22    | ...     | ...     | ...              | ...     |
| 4527             | 0.90                  | ...              | 0.98  | ...    | ...                | 0.45    | ...   | 0.046   | ...                  | 0.30    | ...     | ...     | 0.35             | ...     |
| 4569 *           | 0.78                  | ...              | 0.89  | ...    | ...                | 0.23    | ...   | 0.054   | 0.21                 | 0.12    | 0.06    | ...     | 0.19             | ...     |
| 4666             | 0.65                  | ...              | 0.3:  | ...    | ...                | 0.62    | ...   | 0.040   | ...                  | 0.16    | 0.21    | ...     | 0.10             | ...     |
| 4826 *           | 0.62                  | ...              | 0.75  | ...    | ...                | 0.42    | 0.68  | 0.099   | 0.28                 | 0.22    | 0.15    | 0.36    | 0.13             | ...     |
| 5033 *           | 0.74                  | ...              | ...   | 0.5:   | ...                | 0.84    | ...   | 0.024   | ...                  | 0.94    | ...     | ...     | 0.52             | ...     |
| 5055 *           | 0.55                  | ...              | ...   | ...    | ...                | 0.27    | ...   | 0.046   | ...                  | 0.24    | 0.12    | ...     | ...              | ...     |
| 5194 *           | 0.47                  | ...              | 0.6:  | ...    | ...                | 0.38    | 0.4:  | 0.198   | 0.15                 | 0.13    | 0.10    | ...     | 0.20             | ...     |
| 5236             | 1.22                  | ...              | ...   | ...    | 1.14 <sup>c</sup>  | 0.50    | 0.34  | 0.054   | ...                  | 0.33    | ...     | ...     | ...              | 0.16    |
| 5775             | 0.94                  | ...              | 0.5:  | ...    | ...                | 0.19    | ...   | 0.032   | ...                  | ...     | ...     | ...     | ...              | ...     |
| 6240             | 1.68                  | 1.36             | 0.92  | 0.4:   | 1.65 <sup>d</sup>  | 0.21    | ...   | 0.080   | 1.00                 | 0.75    | 0.58    | ...     | 0.14             | ...     |
| 6701 *           | 1.02                  | ...              | 0.95  | 0.76   | ...                | 0.41    | ...   | 0.052   | ...                  | 0.39    | 0.44    | 0.44    | 0.67             | ...     |
| 6946             | 0.85                  | ...              | 0.93  | 0.83   | 3.21 <sup>d</sup>  | 0.40    | 0.51  | 0.057   | 0.41                 | 0.25    | 0.06    | 0.31    | 0.23             | ...     |
| 6951 *           | 0.74                  | ...              | 1.13  | 1.15   | ...                | 0.56    | 0.59  | 0.071   | 0.87                 | 0.28    | ...     | 0.30    | 0.45             | ...     |
| 7469 *           | 1.05                  | ...              | 0.75  | 0.75   | ...                | 0.52    | 0.5:  | 0.060   | ...                  | 0.57    | 0.18    | ...     | 0.41             | ...     |
| 7771             | 1.05                  | ...              | 0.60  | 2.08   | ...                | 0.43    | 1.02  | 0.081   | ...                  | 0.12    | ...     | 0.28    | 0.31             | ...     |
| A220             | 0.46                  | ...              | 0.25  | ...    | 0.76               | 0.96    | ...   | 0.089   | ...                  | 1.18    | 0.31    | ...     | 0.71             | 0.21    |
| MW <sup>e</sup>  | 0.60                  | ...              | ...   | ...    | ...                | 0.30    | ...   | 0.10    | ...                  | ...     | ...     | ...     | ...              | ...     |
| Ave              | 0.90                  | 1.1              | 0.95  | 1.06   | 1.42               | 0.46    | 0.52  | 0.046   | 0.49                 | 0.41    | 0.27    | 0.34    | 0.42             | 0.29    |
|                  | ±0.05                 | ±0.2             | ±0.10 | ±0.11  | ±0.21              | ±0.03   | ±0.07 | ±0.006  | ±0.08                | ±0.04   | ±0.04   | ±0.05   | ±0.03            | ±0.07   |
| MD <sup>f</sup>  | 0.30                  | 0.40             | 0.52  | 0.47   | 0.82               | 0.17    | 0.24  | 0.039   | 0.27                 | 0.25    | 0.18    | 0.16    | 0.19             | 0.16    |
| Err <sup>g</sup> | 0.05                  | 0.15             | 0.15  | 0.2    | 0.3                | 0.05    | 0.15  | 0.15    | 0.3                  | 0.2     | 0.3     | 0.2     | 0.15             | 0.3     |

Notes: a. Based on *APEX* 12m observations by Zhou et al. (2022). b. Based on *IRAM* observations (HPBW 14'') by Krips et al. (2008). c. Includes *JCMT* observations by Tan et al. (2018). d. From *APEX* 12m observations (HPBW 18'') by F.P. Israel (unpublished) and by Zhang et al. (2014). e. Milky Way Circumnuclear Molecular Zone values from *MOPRA* 22m observations (effective resolution 39'') by Jones et al. (2012). f. Mean deviation of sample. g. Logarithm of typical observational error of ratios plotted in Figures 3-11; individual errors vary depending on observed intensity (cf. Table 3).

#### 4.2. $J=1-0$ HCN/CO and FIR/CO as a function of luminosity

Whereas absolute luminosities are dominated by galaxy distances and shed little light on the physical conditions in the cen-

**Table 7.** Line transition ratios as a function of CO luminosity

| $\log L(\text{CO})^a$<br>$\text{K km s}^{-1}$ | HCN <sup>b</sup>   |                    |                    |                    | HCO <sup>+</sup> <sup>b</sup> |
|---|--------------------|--------------------|--------------------|--------------------|-------------------------------|
| (1)   | (2-1)/(1-0)<br>(2) | (3-2)/(1-0)<br>(3) | (4-3)/(1-0)<br>(4) | (3-2)/(1-0)<br>(5) |                               |
| 7.4   | 0.31 (5)           | 0.25 (9)           | 0.16 (6)           | 0.32 (6)           |                               |
| 8.3   | 0.53 (5)           | 0.41 (16)          | 0.26 (9)           | 0.37 (14)          |                               |
| 8.8   | ...                | 0.68 (14)          | 0.42 (4)           | 0.45 (3)           |                               |
| 9.3   | ...                | 0.35 (9)           | 0.30 (4)           | 0.45 (10)          |                               |
| 9.9   | ...                | 0.67 (6)           | ...                | 0.61 (7)           |                               |
| 7.0-9.0 <sup>c</sup>                          | 0.49 (12)          | 0.40 (29)          | 0.26 (19)          | 0.37 (23)          |                               |
| 7.0-10.0 <sup>c</sup>                         | ...                | 0.43 (44)          | 0.27 (24)          | 0.43 (40)          |                               |

Notes: a. Center of luminosity interval considered; b. Number of points in interval is given between parentheses; entries for intervals with only one point are deleted; c. Range considered for overall average.

tral regions of galaxies, this may be different for luminosity<sup>4</sup> ratios. First, we turn to relations between the HCN(1-0)/CO(1-0) ratio and the CO, HCN, HCO<sup>+</sup>, and FIR luminosities. With some reservations, Gao & Solomon (2004a) interpreted the ratio  $L(\text{HCN})/L(\text{CO})$  as an indicator for the fraction of dense molecular gas in galaxies. They found it to be rather low ( $\leq 0.06$ ) in low-luminosity normal spiral galaxies but dramatically increasing to  $L(\text{HCN})/L(\text{CO}) \sim 0.25$  in high luminosity galaxies  $L(\text{FIR}) \geq 11$ , all galaxies with  $L(\text{HCN})/L(\text{CO}) \geq 0.06$  being (ultra)luminous (Gao & Solomon 2004b). We do not confirm these findings. The more accurate HCN/CO ratios at galaxy central positions shown in Fig. 4 (top left panel) do not exhibit such a jump at high values of  $L(\text{FIR})$  and show the same dispersion at low and high luminosities. The behaviour of HCN/CO as a function of  $L(\text{CO})$  is no different and this is also true if we substitute HCO<sup>+</sup>(1-0) for HCN(1-0). In Fig. 4, there is no systematic correlation between the HCN/CO ratio and either  $L(\text{FIR})$  (top left) or  $L(\text{CO})$  (top right). Similar plots of infrared and molecular line measurements in matching beams presented by Li et al. (2021) likewise fail to reveal correlations between the infrared luminosity and the HCN/IR or HCO<sup>+</sup>/IR ratios. The center left panel of Fig 4 shows at best a weak correlation between  $L(\text{HCN})/L(\text{CO})$  and  $L(\text{HCN})$ , with  $L(\text{HCN})/L(\text{CO}) \propto L(\text{HCN})^{0.1}$ . Substitution of HCO<sup>+</sup> for HCN yields the same result with a slightly lower dispersion. A direct comparison of the present results and those by e.g. Li et al. (2021) with the results published by Gao & Solomon (2004a, b) is not easy because the latter constructed spatially integrated luminosities from heterogeneous data obtained at different resolutions, at lower sensitivities in much narrower bands. It is not entirely clear how they constructed luminosity ratios such as those of HCN to CO. In the combined database presented here, luminous galaxies have on average significantly lower HCN/CO ratios than those listed by Gao & Solomon (2004b), whereas many lower-luminosity galaxies have significantly higher HCN/CO ratios. The two data sets have 39 galaxies in common. For seven (18%) galaxies Gao & Solomon list lower HCN/CO ratios, but for twenty-four (62%) they find (significantly) higher ratios. It is noteworthy that almost all of these refer to (luminous) galaxies with wide lines of low-amplitude, filling most of the observed spectral window and leaving little room for accurate baseline-fitting. We suspect that, as a result, Gao & Solomon have overes-

timated the corresponding HCN luminosities, and that the more recently obtained data supersede these older values.

In a similar way, the ratio  $L(\text{FIR})/L(\text{CO})$  is often presented as a proxy for the star formation efficiency (more correctly: the inverse of the molecular gas depletion rate), under the assumption that  $L(\text{FIR})$  is proportional to the star formation rate. We find, however, that the ratio  $L(\text{FIR})/L(\text{CO})$  is uncorrelated with the luminosities  $L(\text{CO})$ ,  $L(\text{HCN})$  or  $L(\text{HCO}^+)$ , and only shows a weak correlation with  $L(\text{FIR})$  with a modest logarithmic slope  $\sim 0.13$  (Fig. 4, center right). It is not clear whether this is a slow increase over the full range of  $\log L(\text{FIR})$  or a rise only at values  $\log L(\text{FIR}) \geq 11$  of the luminous galaxies. Graciá-Carpio et al. (2009) found a similar weak correlation between  $L(\text{FIR})/L(\text{HCN})$  and  $L(\text{FIR})$  with a logarithmic slope 0.24 for (ultra)luminous galaxies. The larger sample studied here does not show such a correlation between either  $L(\text{FIR})/L(\text{HCN})$  or  $L(\text{FIR})/L(\text{HCO}^+)$  and  $L(\text{FIR})$ .

Gao & Solomon (2004b) found the ‘star formation efficiency’  $L(\text{FIR})/L(\text{CO})$  to be strongly correlated with the ‘dense gas fraction’  $L(\text{HCN})/L(\text{CO})$ . We find a similar but weaker relation in the bottom left panel of Fig. 4. Gao & Solomon did not find a relation between  $L(\text{FIR})/L(\text{CO})$  and  $L(\text{FIR})/L(\text{HCN})$ , but our data reveal these quantities to be well-correlated (Fig. 4, bottom right), even though  $L(\text{FIR})/L(\text{HCN})$  and  $L(\text{CO})$  are not. In these bottom panels there is no systematic difference between normal galaxies, starburst galaxies and AGNs.

Neither  $L(\text{HCN})/L(\text{CO})$  nor  $L(\text{FIR})/L(\text{CO})$  is correlated with distance  $D$ . Hence, they also do not depend on the extent of the central area sampled.

#### 4.3. Dense and very dense molecular gas: HCO<sup>+</sup>(1-0) and HCN(1-0)

The relation between the dense gas supposedly traced by HCO<sup>+</sup> and the very dense gas traced by HCN is of further interest, especially since their ground state intensities are derived from the same observed profiles so that their ratio is free of systematic uncertainties and thus quite accurate. Despite critical densities an order of magnitude apart, the  $J=1-0$  HCO<sup>+</sup> and HCN luminosities are closely related and practically interchangeable. Graciá-Carpio et al. (2008) claimed a correlation between the ground-state HCN-to-HCO<sup>+</sup> ratios and the infrared luminosities of (U)LIRGs but Privon et al. (2015) could not confirm this, nor can we. The present data extending over a three times larger luminosity range clearly establish that HCN/HCO<sup>+</sup> ratios are not related to either FIR or CO luminosities (Fig. 5 left panel), nor to CO intensities. The average HCN-to-HCO<sup>+</sup> ratio of 1.1 is constant and slightly above unity. The same behavior is also found on smaller scales, such as the central kilo-parsec of NGC 253 (Knudsen et al. 2007). In the  $J=2-1$  (Zhou et al. 2022),  $J=3-2$  and  $J=4-3$  (This paper, Zhang et al. 2014, Imanishi et al. 2018) transitions the average ratios are 0.9, 1.0, and 0.7, respectively. The ratios of the first three transitions are within each others errors but the  $J=4-3$  ratio is significantly lower. When the luminosity distance bias is eliminated, for instance by weighting both HCN and HCO<sup>+</sup> by their corresponding CO luminosities, HCO<sup>+</sup>/CO increases somewhat more slowly than HCN/CO with a logarithmic slope  $\sim 0.6$  as shown in Fig 5 (center left panel). There, low-luminosity normal galaxies and high-luminosity LIRGs do not define distinct or separate groups, in line with the absence of correlations between CO luminosity and the ratios of HCN to CO and HCO<sup>+</sup> to CO in Fig. 4. Finally, the center right panel shows that the ‘very-dense-to-dense gas’ ratio  $J=1-0$  HCN/HCO<sup>+</sup> is unrelated to the ‘dense-to-modestly-dense

<sup>4</sup> In identical apertures, there is no meaningful distinction between intensity ratios and luminosity ratios, and we will use both terms interchangeably

gas' ratio HCO<sup>+</sup>/CO, and the rightmost panel shows that there is no correlation between the HCO<sup>+</sup>/HCN and FIR/CO either.

#### 4.4. HCN, HCO<sup>+</sup>, and the <sup>12</sup>CO/<sup>13</sup>CO ground-state ratio

The observed isotopological ratio  $I(^{12}\text{CO})/I(^{13}\text{CO})$  depends on both the intrinsic isotopic abundance ratio and the CO optical depth. The magnitude of the isotopic abundance ratio in galaxy centers is poorly known and estimates range from very low values of 20-40 to high values of 70-150 (see, for instance, the compilation by Viti et al. 2020). Moreover, they may vary from galaxy to galaxy. The present database contains measurements of the isotopological ratio for the majority of galaxies (see Section 3.1). <sup>12</sup>CO(1-0)/<sup>13</sup>CO(1-0) ratios increase both with the CO luminosity  $L(\text{CO})$  (Fig 6 leftmost panel) and with the far-infrared luminosity  $L(\text{FIR})$ . Ratios range from 6-14 at the lowest luminosities and from 10-50 at the highest luminosities. Fig. 6 illustrates that the ratio of HCN-to- HCO<sup>+</sup> decreases as a function of <sup>12</sup>CO/<sup>13</sup>CO (rightmost panel) whereas the 'dense-gas ratio' HCN/CO does not (center left panel) nor does the ratio HCO<sup>+</sup>/CO. Likewise, no relation is found between the 'star-formation-efficiency' FIR/CO and the isotopological ratio (center right panel).

#### 4.5. The ground-state HNC/HCN isomer ratio

The HCN isomer HNC(1-0) was detected by Hüttemeister et al. (1995) in fifteen normal galaxies and mapped in five with the *IRAM* 30m telescope. They determined the isomer ratios by using older HCN measurements. Aalto et al. (2002) presented a complementary HNC(1-0) survey of nine luminous infrared galaxies, obtained with the relatively large beams of the *OSO* (42'') and *SEST* (55'') telescopes. The survey of 23 galaxies by Costagliola et al. (2011), also incorporated into our database, covered a variety of molecular lines in the 3mm window, including HCN(1-0) and HNC(1-0). In all surveys, the ground-state isomer ratio HNC/HCN varies significantly from galaxy to galaxy. A strong motivation for HCN and HNC observations is the potential use of their ratio as a diagnostic for molecular gas kinetic temperature and density (Schilke et al. 1992, Graninger et al. 2014), specifically sensitive to UV but not X-ray irradiation (Bublitz et al. (2019, 2022)). As in the previous smaller samples, the HNC/HCN ratios of the more than ninety galaxies presented here are all in the range 0.2–1.1; the average is 0.46 (Table 6). There is no correlation with global far-infrared luminosity (also noted by Aalto et al. 2002), nor with CO luminosity. Hüttemeister et al. (1995) did not find a correlation with putative tracers of star formation rate or dust temperature. In our much larger sample, the HCN/HNC ratio is wholly unrelated to either the HCN/CO ratio or the HCN/FIR ratio. We confirm the anti-correlation found by Costagliola et al. (2011) between the HCO<sup>+</sup>/HCN and the HNC/HCN ratios when they are plotted against the HNC/HCO<sup>+</sup> ratio (Fig. 7, bottom panels) but unlike these authors we see no relation when they are plotted against each other or sorted by galaxy type (Fig. 7 center right panel). We did not find any other correlation involving the isomer ratio.

#### 4.6. The excitation ladders of HCN, HCO<sup>+</sup> and HNC

The normalized  $J=3-2$  HCN and HCO<sup>+</sup> luminosities are, just like the ground-state luminosities, well-correlated with the  $J=1-0$  CO luminosities. The super-unity slope of about 1.12 is iden-

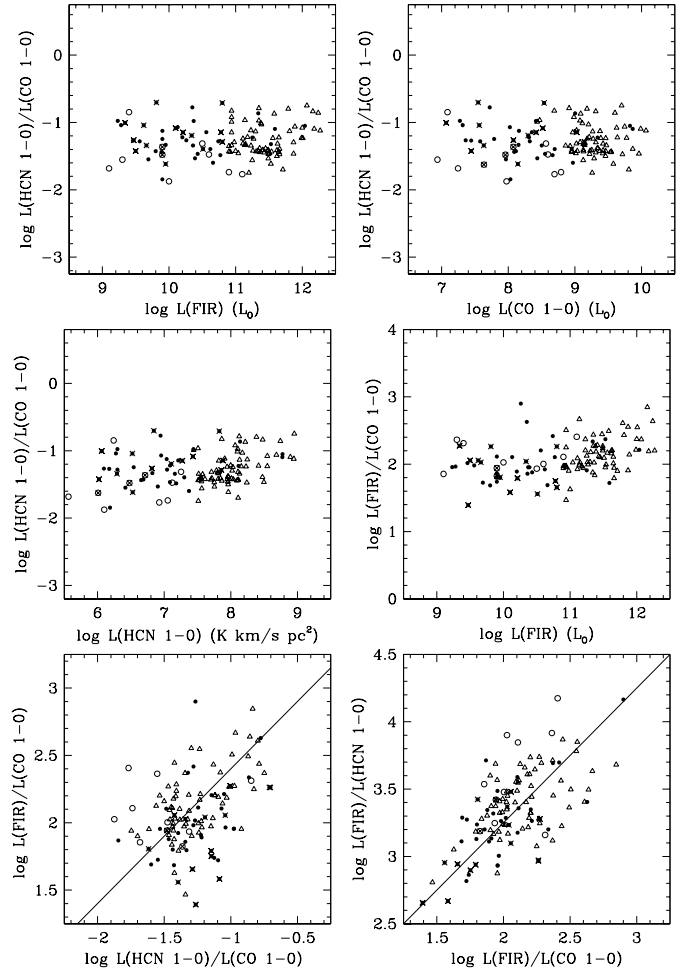


**Fig. 4.** Top row: the  $J=1-0$  HCN/CO ratio as a function of *IRAS* FIR luminosity (left) and  $J=1-0$  CO luminosity (right). The horizontal line in the panel at left marks the ratio separating normal and luminous galaxies in the paper by Gao & Solomon (2004b). Neither panel shows any increase in HCN/CO at (U)LIRG luminosities, nor any change in the dispersion of the ratio. Center row: The HCN/CO ratio as a function of  $L(\text{HCN})$  (left) and the FIR/CO ratio as a function of  $L(\text{FIR})$  (right). Bottom row: The FIR/CO ratio versus HCN/CO ratio (left); the FIR/HCN ratio versus the FIR/CO ratio (right). In both panels, straight lines mark unity slopes. Fit parameters are listed in Table 8.

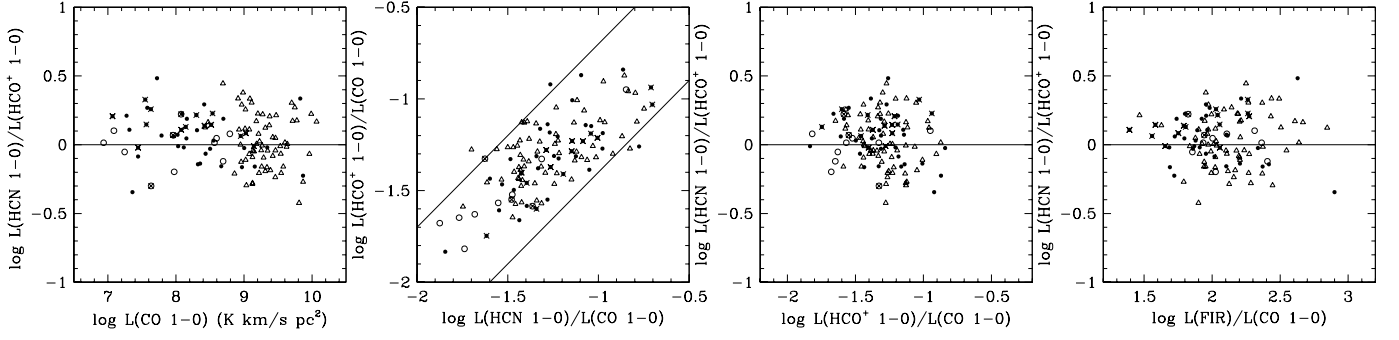


**Fig. 5.** Left: The HCN-to-  $\text{HCO}^+$  versus the FIR-to-CO luminosity ratio. The horizontal line marks equal HCN and  $\text{HCO}^+$  luminosities. Center: The  $\text{HCO}^+/\text{CO}$  versus the HCN/CO luminosity ratio. Right: The  $\text{HCO}^+/\text{HCN}$  versus the HCN/CO luminosity ratio. The solid line has slope -0.55. Fit parameters are listed in Table 8.

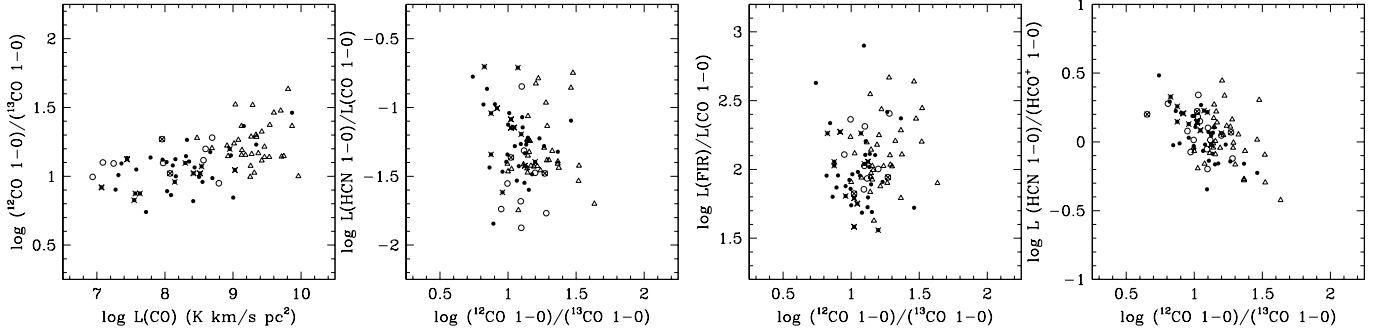


**Fig. 6.** From left to right, the ground-state isotopologue  $^{12}\text{CO}/^{13}\text{CO}$  ratio as a function CO luminosity and the HCN/CO, FIR/CO, and HCN/  $\text{HCO}^+$  ratios as a function of the  $^{12}\text{CO}/^{13}\text{CO}$  ratio. Fit parameters are listed in Table 8.

tical to the slope of 1.11 found by Li *et al.* (2020) for the relation between HCN(3-2) and FIR luminosities in matched apertures, and less than the more poorly defined slope of 1.26-1.35 found by Bussman *et al.* (2008) in the larger HST beam. In Fig. 8 the individual HCN(2-1) (taken from Krips *et al.* 2008), HCN(3-2), HCN(4-3), and HNC(3-2) intensities relative to the ground-state are plotted as a function of the CO(1-0) luminosity. With increasing transition the average line intensities drop (columns 9-11 in Table 6, and Fig. 8). Using that figure to remove the bias due to unequal sampling, we find that the average intensities of the HCN excitation ladder are represented by the series 1.00:0.65:0.45:0.25 which is steeper than the comparable CO ladder of 1.00:0.92:0.70:0.57 (Israel 2020). The averages for  $\text{HCO}^+$  are practically identical (Table 6) columns 13-14). In all  $J$  transitions, individual HCN and  $\text{HCO}^+$  line intensities are very similar (Fig. 9). Because of the paucity of especially JCMT  $J=4-3$   $\text{HCO}^+$  observations, we added to this figure line ratios from the ALMA observations of compact (ultra)luminous galaxies from Imanishi *et al.* (2018) and the APEX observations of normal galaxies from Zhang *et al.* (2014). The APEX  $J=4-3$  and JCMT  $J=3-2$  beams are almost identical facilitating the construction of  $J=4-3/J=3-2$  ratios.

With each additional step on the ladder, average HCN and  $\text{HCO}^+$  intensities decrease but within each step, individual ratios rise with increasing CO luminosity (Table 7, Fig 8). The  $J=1-0$ ,  $J=3-2$ , and  $J=4-3$  intensities HCN and  $\text{HCO}^+$  increase in tandem (leftmost panels in Fig. 9). In each transition, their ratio is a constant and unrelated to either CO (rightmost panels in Fig. 9 or FIR luminosity (Tan *et al.* 2018).

A similar lack of correlation characterizes the HCN/HNC ratios in the two transitions. Again the spread in the  $J=3-2$  values is about double that in the  $J=1-0$  values but the small sample reveals no distinction between AGNs and starburst. In Figs. 5 and 6 we found the  $\text{HCO}^+(1-0)/\text{HCN}(1-0)$  species ratio to be inversely correlated with both the ‘dense-gas fraction’  $\text{HCN}(1-0)/\text{CO}$  and the isotopologue ratio  $^{12}\text{CO}/^{13}\text{CO}$  but independent from the CO luminosity and the ‘star formation efficiency’  $\text{FIR}/\text{CO}$ . The excitation of HCN (and  $\text{HCO}^+$ ) is also unrelated to any of these quantities as illustrated by plots of the  $J=3-2/J=1-0$  ratios against them. Fig. 10 shows that the excitation of HCN is not meaningfully related to the isotopological  $^{12}\text{CO}/^{13}\text{CO}$  ratio (left panel) or to HCN/CO (not shown) and FIR/CO (right panel). Finally, Fig. 11 shows that the excitation of HNC is not related to the luminosities of HCN (left panel) or

**Table 8.** Linear regression fits to luminosities and ratios plotted in Figs. 3 through 11

| y<br>(1)                           | x<br>(2)                           | a<br>(3) | b<br>(4) | rms<br>(5) | sfcc<br>(6) | Reference |
|------------------------------------|------------------------------------|----------|----------|------------|-------------|-----------|
| L(CO)                              | L(HCO <sup>+</sup> )               | 1.03     | -1.60    | 0.21       | 0.95        | Fig. 3    |
| L(CO)                              | L(HCN)                             | 0.99     | -1.16    | 0.25       | 0.92        |           |
| L(CO)                              | L(HNC)                             | 1.02     | -1.83    | 0.29       | 0.94        |           |
| L(FIR)                             | L(HCN)                             | 0.90     | -2.26    | 0.28       | 0.92        |           |
| L(FIR)                             | L(CO)                              | 0.88     | -0.72    | 0.25       | 0.93        |           |
| L(HCN)                             | L(HCO <sup>+</sup> )               | 1.01     | -0.11    | 0.18       | 0.97        |           |
| L(HNC)                             | L(HCN)                             | 0.95     | 0.71     | 0.15       | 0.98        |           |
| I(HNC)                             | I(HCN)                             | 1.97     | 0.43     | 1.87       | 0.91        |           |
| I(HCN)                             | I(HCO <sup>+</sup> )               | 0.86     | 0.15     | 2.24       | 0.88        |           |
| D <sup>2</sup>                     | L(HCN)                             | 0.71     | 5.23     | 0.34       | 0.91        |           |
| D <sup>2</sup>                     | I(HCN)                             | -0.29    | 1.28     | 0.34       | -0.61       |           |
| L(HCN)                             | I(HCN)                             | -0.14    | 1.39     | 0.43       | -0.27       |           |
| L(CO)                              | L(HCN)/L(CO)                       | -0.02    | -1.08    | 0.25       | -0.06       | Fig. 4    |
| L(HCN)                             | L(HCN)/L(CO)                       | 0.09     | -1.92    | 0.24       | 0.27        |           |
| L(FIR)                             | L(HCN)/L(CO)                       | 0.02     | -1.54    | 0.25       | 0.06        |           |
| L(FIR)                             | L(FIR)/L(CO)                       | 0.13     | 0.72     | 0.25       | 0.39        |           |
| L(HCN)/L(CO)                       | L(FIR)/L(CO)                       | 0.43     | 2.63     | 0.25       | 0.38        |           |
| L(FIR)/L(CO)                       | L(FIR)/L(HCN)                      | 0.64     | 2.03     | 0.23       | 0.53        |           |
| L(CO)                              | L(HCN)/L(HCO <sup>+</sup> )        | -0.05    | 0.48     | 0.17       | -0.22       |           |
| L(HCN)/L(CO)                       | L(HCO <sup>+</sup> )/L(CO)         | 0.59     | -0.51    | 0.15       | 0.69        |           |
| L(HCO <sup>+</sup> )/L(CO)         | L(HCN)/L(CO)                       | -0.14    | -0.15    | 0.18       | -0.17       | Fig. 5    |
| L(FIR)/L(CO)                       | L(HCN)/L(HCO <sup>+</sup> )        | -0.00    | 0.04     | 0.18       | -0.01       |           |
| L(CO)                              | <sup>12</sup> CO/ <sup>13</sup> CO | 0.12     | 0.08     | 0.14       | 0.58        |           |
| <sup>12</sup> CO/ <sup>13</sup> CO | L(HCN)/L(CO)                       | -0.29    | -0.98    | 0.25       | -0.12       |           |
| <sup>12</sup> CO/ <sup>13</sup> CO | L(FIR)/L(CO)                       | 0.18     | 1.85     | 0.25       | 0.15        |           |
| <sup>12</sup> CO/ <sup>13</sup> CO | L(HCN)/L(HCO <sup>+</sup> )        | -0.55    | 0.66     | 0.15       | -0.43       |           |
| <sup>12</sup> CO/ <sup>13</sup> CO | L(HCN)/L(HNC)                      | 0.06     | 2.26     | 0.87       | -0.07       |           |
| L(FIR)                             | L(HCN)/L(HNC)                      | -0.08    | 3.20     | 0.87       | -0.14       |           |
| L(CO)                              | L(HNC)/L(HCO <sup>+</sup> )        | -0.06    | 2.82     | 0.87       | -0.13       | Fig. 7    |
| L(HNC)/L(CO)                       | L(HCN)/L(HNC)                      | -0.26    | 0.08     | 0.14       | -0.47       |           |
| L(HNC)/L(HCN)                      | L(HCO <sup>+</sup> )/L(HCN)        | -0.05    | -0.06    | 0.17       | -0.02       |           |
| L(HNC)/L(HCO <sup>+</sup> )        | L(HCO <sup>+</sup> )/L(HCN)        | -0.54    | -0.20    | 0.12       | -0.74       |           |
| L(HNC)/L(HCO <sup>+</sup> )        | L(HNC)/L(HCN)                      | 0.46     | -0.20    | 0.12       | 0.66        |           |
| L(CO)                              | HCO <sup>+</sup> (3-2)/(1-0)       | 0.12     | -1.37    | 0.25       | 0.32        |           |
| L(CO)                              | HCN(2-1)/(1-0)                     | 0.21     | -2.08    | 0.18       | 0.64        |           |
| L(CO)                              | HCN(3-2)/(1-0)                     | 0.17     | -1.81    | 0.21       | 0.46        |           |
| L(CO)                              | HCN(4-3)/(1-0)                     | 0.23     | -2.61    | 0.25       | 0.47        | Fig. 9    |
| HCN(3-2)/(1-0)                     | HCO <sup>+</sup> (3-2)/(1-0)       | 0.57     | -0.14    | 0.17       | 0.68        |           |
| HCN(4-3)/(3-2)                     | HCO <sup>+</sup> (4-3)/(3-2)       | 0.70     | 0.03     | 0.11       | 0.70        |           |
| L(CO)                              | J=3-2 HCO <sup>+</sup> /HCN        | 0.14     | -0.15    | 0.24       | 0.17        |           |
| L(CO)                              | J=4-3 HCO <sup>+</sup> /HCN        | 0.08     | -0.68    | 0.32       | 0.13        |           |
| <sup>12</sup> CO/ <sup>13</sup> CO | HCN(3-2)/(1-0)                     | 0.32     | -0.71    | 0.23       | 0.16        |           |
| L(FIR)/L(CO)                       | HCN(3-2)/1-0                       | -0.34    | 0.33     | 0.22       | -0.38       |           |
| L(HCN)                             | HNC(3-2)/(1-0)                     | 0.07     | -1.02    | 0.24       | 0.18        |           |
| HCN(3-2)/(1-0)                     | HCN/HNC(1-0)                       | -0.16    | 0.30     | 0.15       | -0.18       | Fig. 11   |

Notes: a. The regression fits are of the form  $\log(y) = a \log(x) + b$ . Columns 1 and 2 identify the data used in the fit. Column 3 and 4 list the slope  $a$  and  $y$ -axis intercept of the fitted relation. Column 5 lists the r.m.s. residuals of the fit; the observed dispersion exceeds the observational error, and the physical range of the  $y$ -parameter is about four times the quoted r.m.s. Column 6 gives the Spearman correlation coefficient of the fit, ranging from -1.00 (perfect anti-correlation) to 1.00 (perfect correlation). Coefficients in the range -0.35 to +0.35 should be interpreted as indicating a lack of correlation, especially when slope  $a$  is also close to zero.

CO, and that the HCN/HNC isomer and the HCN(3-2)/HCN(1-0) excitation ratio are likewise unrelated.

## 5. Discussion

### 5.1. Luminosity plots provide little information

The results in this paper confirm that the linear relations between the HCN(1-0), CO(1-0), and FIR luminosities of whole galaxies, first established by Solomon et al. (1992) and Gao & Solomon

(2004a), also hold for constant aperture measurements of galaxy centers. They also show that the surface brightness of CO, HCN, and HCO<sup>+</sup> drops in similar ways when the area covered by the aperture increases. Variations in surface brightness and intensity ratios are almost negligible compared to the variation in galaxy distances. Distance is the single factor dominating the luminosities in fixed apertures. This is the key factor explaining the near-linearity of luminosity-luminosity relations and it also explains why luminosity correlations look progressively better as greater ranges in distance are considered. As a result, the luminosity-

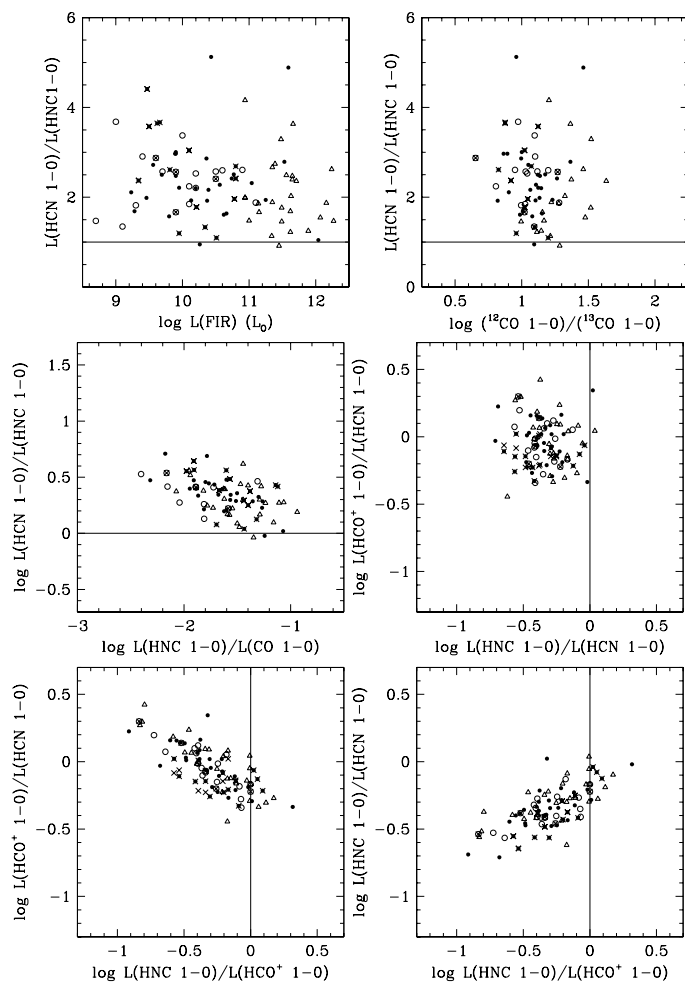


**Fig. 7.** Top: the ground-state HCN/HNC isomer ratio as a function of FIR luminosity (left) and the  $^{12}\text{CO}/^{13}\text{CO}$  isotopologue ratio (right). Center: the ground-state HCN/CO (left) and  $\text{HCO}^+/\text{HCN}$  (right) ratios as a function of the (inverse) HNC/HCN isomer ratio. Bottom: the ground-state  $\text{HCO}^+/\text{HCN}$  (left) and HNC/HCN (right) ratios as a function of the HNC/ $\text{HCO}^+$  ratio. Solid lines mark unity isomer ratios. Fit parameters are listed in Table 8.

luminosity relations published in the literature, and also presented here, are mostly trivial and provide very little information on the physical properties of the galaxies sampled<sup>5</sup>. Specifically, the observation that linear luminosity relations hold over a wide range of luminosities does not provide evidence that the extragalactic star formation rate is directly proportional to the mass of dense gas. The scatter in the various luminosity-luminosity plots carries more information than their linearity. The non-negligible dispersion involves factors of five or more and indicates significant variation among individual galaxies even as a systematical change with luminosity is absent. Intensity ratios provide a much better means of evaluating the information conveyed by molecular line emission than luminosities.

The luminosity plots do not reveal systematical differences between the various galaxy types either. The only exception

is the  $\text{HCO}^+$  intensity which is always below that of HCN in AGN galaxies. Over the observed range  $9.0 \leq \log L(\text{FIR}) (L_\odot) \leq 12.5$ , the linearity of the various CO, HCN, or  $\text{HCO}^+$  luminosity relations does, however, imply that interstellar medium (ISM) properties do not change as a function of galaxy luminosity.

## 5.2. HCN and $\text{HCO}^+$ trace the same gas

The average  $J=1-0$   $\text{HCO}^+$  to HCN intensity ratio is about 0.9 but individual values can be up to three times higher or lower. The behavior of  $\text{HCO}^+$  and HCN is practically the same in all observed transitions (Fig. 9) which implies that both molecules essentially trace the same gas, even at the higher critical densities. Over a wide range of luminosities, the central regions of other galaxies are thus much like the inner Milky Way, where Evans et al. (2020) found that HCN(1-0) and  $\text{HCO}^+(1-0)$  both seem to probe the same molecular cloud material. When large areas are sampled instantaneously, as in extra-galactic measurements, the integrated HCN or  $\text{HCO}^+$  emission from ensembles of molecular gas clouds is easily dominated by extended regions of low density, down to  $10^2 \text{ cm}^{-3}$  (Evans et al. 2020). This may go some way to explain the similar behavior of the emission from HCN and  $\text{HCO}^+$ , as well as CO, notwithstanding the different critical densities sampled (Table 1). From a practical point of view, in most of the analysis HCN and  $\text{HCO}^+$  are interchangeable molecular species.

AGNs do have systematically higher HCN/ $\text{HCO}^+$  ratios than star-burst galaxies (Kohno et al. 2001, 2008; Imanishi et al. 2007; Krips et al. 2008, Gracia-Carpio et al. 2008, and various later papers). As HCN/CO ratios also appeared to be higher in AGN-dominated galaxies, these authors concluded to an HCN over-luminosity reflecting an HCN overabundance. Figs. 4 and 5 confirm that ground-state HCN intensities exceed those of  $\text{HCO}^+$  in all AGN galaxies (except NGC 4258, Li et al. 2019) unlike star-burst galaxies. The situation is complicated by overlooked AGNs, embedded in ULIRGs (Imanishi et al. 2007, Imanishi 2009, Li et al. 2021). High-resolution observations such as provided by ALMA may bring to light significant small-scale variation that is smoothed out in the larger-beam observations considered here. AGNs such as those in e.g. NGC 7469 (Izumi et al. 2020) and NGC 1068 (Butterworth et al. 2022) become manifest by the change in line behavior in their immediate ( $\sim 100 \text{ pc}$ ) surroundings. Fig. 9 includes the HCN/ $\text{HCO}^+$  ratios of distant ULIRGS ( $12.0 \leq \log L(\text{FIR}) \leq 12.3$ ) in the  $J=3-2$  and  $J=4-3$  transitions observed with ALMA (Imanishi et al. 2018). The distinction between AGN and starburst galaxies is less obvious in the higher transitions. In these galaxies, however, the compact nuclear regions (diameter  $\leq 500 \text{ pc}$ ) have again higher HCN/ $\text{HCO}^+$  ratios than the surrounding extended regions.

Attempts to explain high HCN/ $\text{HCO}^+$  ratios by analyzing the few observed optically thick molecular lines in terms of star formation or (X-ray) chemistry with radiative transfer models failed to produce conclusive results (cf. Costagliola et al. 2011, Izumi et al. 2016, Imanishi et al. 2016, Privon et al. 2020). We expect such modelling to be successful only when molecular species are selected specifically capable of diagnostically distinguishing different excitation mechanisms and, as in the case of CO (Israel 2020), only when multiple transitions, including optically thin lines in addition to optically thick lines, are considered.

Although the AGNs in our large sample have systematically higher HCN(1-0)/ $\text{HCO}^+(1-0)$  ratios, they do not have systematically higher ratios HCN(1-0)/CO(1-0) (Fig. 4), and Aladro et al. (2015) found that their HCN(1-0)/CS(3-2) ratios are not system-

<sup>5</sup> see also Kennicutt (1990)

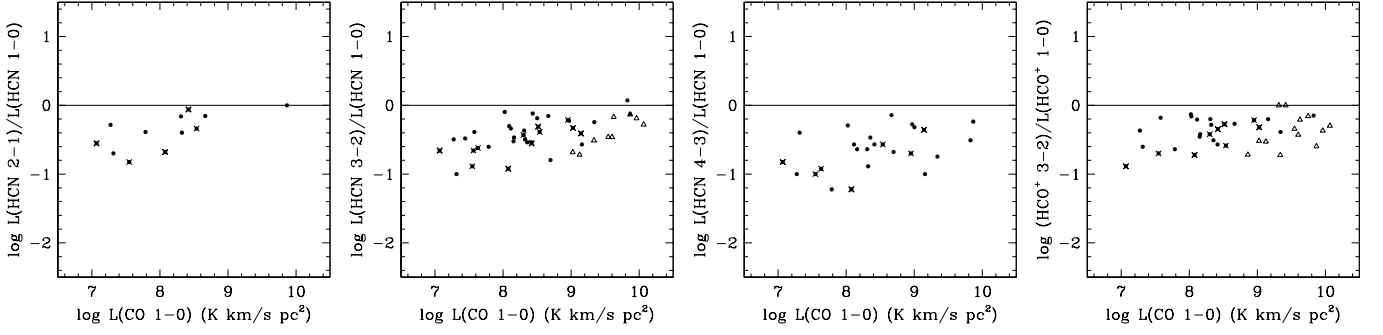


**Fig. 8.** Molecular line ladders: the HCN and HCO<sup>+</sup> line intensity ratios as a function of transition in normalized (equal) beams. Left to right: the HCN  $J=2-1/J=1-0$ ,  $J=3-2/J=1-0$ ,  $J=4-3/J=1-0$ , and the HCO<sup>+</sup>  $J=3-2/J=1-0$  ratios as a function of <sup>12</sup>CO  $J=1-0$  luminosity. Solid lines mark ratios of unity. Symbols are as in Fig.3 but almost all data are from this paper. Fit parameters are listed in Table 8.

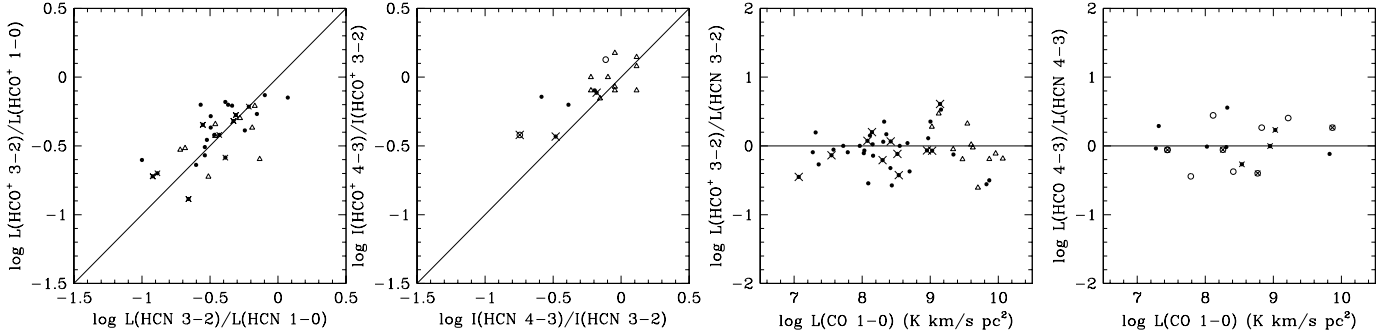


**Fig. 9.** The leftmost two panels ratios illustrate the similarity of the HCO<sup>+</sup> and HCN ladders. The rightmost panels show that the HCO<sup>+</sup>/HCN intensity ratios remain constant over the full range of  $J=1-0$  CO luminosities. The  $J=4-3$  data shown include data from APEX and ALMA in addition to the IRAM data from this paper. Straight lines mark ratios of unity. Fit parameters are listed in Table 8.

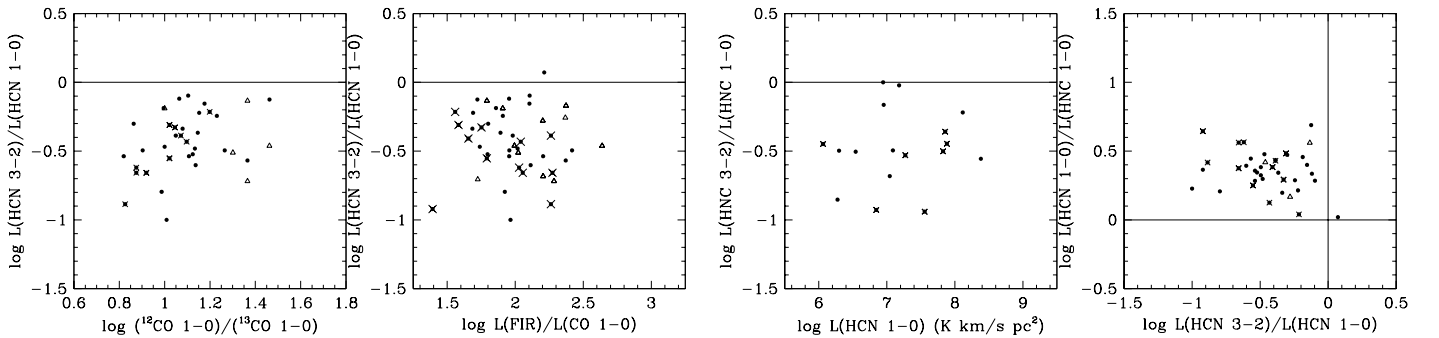


**Fig. 10.** Comparison of the  $J=3-2/J=1-0$  HCN ratio as a function of the isotopological ratio <sup>12</sup>CO/<sup>13</sup>CO (leftmost panel) and FIR/CO (rightmost panel). Solid lines mark ratios of unity. Symbols are as in Fig.3. Fit parameters are listed in Table 8.

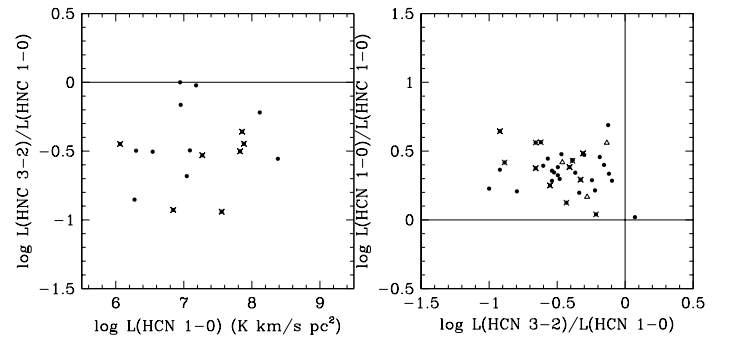


**Fig. 11.** Left: the HNC(3-2)/HNC(1-0) excitation ratio as a function of the HCN(1-0) luminosity. The ground-state HCN/HNC ratio as a function of the HCN(3-2)/HCN(1-0) excitation ratio. Solid lines mark ratios of unity. Symbols are as in Fig.3; most data are from this paper. Fit parameters are listed in Table 8.

atically higher, either. This suggests that in AGNs,  $\text{HCO}^+$  is suppressed rather than HCN enhanced. This suggestion is shared, on different grounds, by Imanishi et al. (2022). Papadopoulos (2007) has argued that environmental conditions differently affecting the chemistries of ions and neutral molecules naturally lead to  $\text{HCO}^+$  suppression. For instance, in the turbulent molecular clouds that dominate in galaxy centers (cf. Israel 2020), free electrons from the ionized outer layers are transported inwards, effectively suppressing the  $\text{HCO}^+$  ion in addition to exciting HCN. Better understanding requires a greater variety of diagnostic line measurements to constrain models. In the absence of independent evidence whether  $\text{HCO}^+$  or HCN is primarily affected by AGN environments, any conclusion obtained from modelling is bound to remain speculative.

### 5.3. Modest optical depths suggest large translucent fraction

Decreases in optical depth  $\tau$  and in isotopic abundance ratio  $[\text{HCO}^+]/[\text{HNC}]$  both express themselves through increasing isotopologue intensity ratios  $I(^{12}\text{CO})/I(^{13}\text{CO})$ . The observed isotopologue ratios increase with CO luminosity (Fig. 6, left panel) as well as FIR luminosity. This may be due to (a), significant carbon monoxide photo-dissociation, (b), selective  $^{12}\text{CO}$  nucleosynthesis, or (c), both. (a), Photo-dissociation of CO in the strong radiation fields of luminous galaxies would diminish the optical depths of both  $^{12}\text{CO}$  ( $\tau_{12\text{CO}}$ ) and  $^{13}\text{CO}$  ( $\tau_{13\text{CO}}$ ) and cause the observed line ratio to approach the isotopic abundance ratio, which itself may increase with luminosity (Visser et al. 2009). Because luminous galaxies are actively forming stars, low optical depths  $\tau_{12\text{CO}}$  signify low abundances  $[\text{HCO}^+]/[\text{H}_2]$  rather than low overall ISM optical depths. (b) Whereas selective photo-dissociation of  $^{13}\text{CO}$  appears to be unimportant (Visser et al. 2009, Romano et al. 2017), selective nucleosynthesis of  $^{12}\text{CO}$  may occur in star-forming galaxies rendering  $^{12}\text{CO}$  overabundant (Sage et al. 1991; Wilson 1999; Romano 2017). Thus,  $\tau_{12\text{CO}}$  would increase with respect to  $\tau_{13\text{CO}}$ . The increased aperture filling fraction of optically thick emission raises observed  $^{12}\text{CO}$  intensity relative to  $^{13}\text{CO}$  intensity.

The observed HCN-to-CO or FIR-to-CO ratios do not correlate with the  $I(^{12}\text{CO})/I(^{13}\text{CO})$  isotopologue ratio. This argues against (b), because enhanced CO intensities would depress these ratios, and supports (a) where  $^{12}\text{CO}$  intensities do not fall with decreasing optical depths as long as  $\tau_{12\text{CO}} \geq 1$ . Inferred optical depths decrease from  $\tau_{13\text{CO}} \approx 0.08 - 0.13$  for the low-luminosity galaxies to  $\tau_{13\text{CO}} \approx 0.03 - 0.07$  for the luminous galaxies. For isotopic abundance ratios of 40, typical for nearby galaxy centers (cf. Viti et al. 2020) these correspond to  $\tau_{12\text{CO}} \approx 3 - 5$  (low luminosity) and  $\tau_{12\text{CO}} \approx 1 - 3$  (high luminosity). For typical luminous galaxy isotopic abundances 100 (cf. Viti et al. 2020), the corresponding  $\tau_{12\text{CO}} \approx 3 - 8$  is similar to that of low-luminosity galaxies. It appears that the ground-state lines of our sample are just optically thick with optical depths of a few. The modest CO optical depths represent averages over relatively large surface areas and suggest that the ensemble of molecular clouds sampled contains a significant fraction of translucent clouds in addition to more dense clouds. In the environments sampled, low CO optical depths do not imply equally low molecular hydrogen column densities  $N(\text{H}_2)$  (cf. Israel 2020). Optical depths of the very weak  $J=1-0$   $\text{H}^{13}\text{CN}$ ,  $\text{H}^{13}\text{CO}^+$ , and  $\text{HN}^{13}\text{C}$  lines have been determined for a small number of bright galaxies (Nguyen-Q-Rieu et al. 1992, Costagliola et al. 2011, Jiang et al. 2011, Aladro et al. 2015, Jiménez-Donaire et al. 2017, Li et al. 2019, 2020b). Optical

depths  $\tau_{\text{H}^{13}\text{CN}}$  are typically 0.02-0.15 with higher values 0.25-0.35 for some LIRGs such as NGC 1614 and UGC 05101. Optical depths  $\tau_{\text{H}^{13}\text{CO}}$  are in the range 0.02-0.10, not very different from either  $\tau_{\text{H}^{13}\text{CN}}$  or  $\tau_{13\text{CO}}$ . These low optical depths likewise suggest that a non-negligible fraction of the emission in these lines comes from translucent gas. As already referred to in the previous section, HCN(1-0) emission from Milky Way molecular clouds is easily detected also in extended translucent regions with densities  $N(\text{H}_2) \sim 500 \text{ cm}^{-3}$  (Pety et al. 2017, Evans et al. 2020). At low  $^{13}\text{CO}$  optical depths, the HCN/ $\text{HCO}^+$  intensity ratio drops to values below unity (Fig. 6, right panel). In that case, a larger fraction of the molecular gas in luminous galaxies is at reduced (column) densities better traced by  $\text{HCO}^+$  than by HCN.

### 5.4. The dense molecular gas is lukewarm

The model calculations by Schilke et al. (1992) illustrate how the HCN/HNC ratio increases with rising molecular gas kinetic temperature and density, presumably caused by temperature-dependent destruction of HNC in neutral-neutral reactions. Despite the degeneracy between temperature and density, the analysis of observations in Orion allowed Hacar et al. (2020) to derive an empirical relation between the HCN/HNC ratio and the independently determined kinematic gas temperature. The ratios  $I(\text{HCN})/I(\text{HNC}) = 1-5$  observed by us are in the well-established part of the relation in their Figure 3, where  $T_{\text{kin}} \approx 10 \times I(\text{HCN})/I(\text{HNC})$ . Thus, the kinetic temperatures of the HCN gas in the sample galaxies are  $T_{\text{kin}} = 10 - 50 \text{ K}$ , with a mean of 20 K. These are beam-averaged temperatures; a temperature of 20 K might, for instance, also represent a mixture of 25 per cent gas at 50 K and 75 per cent gas at 10 K etc. The absence of ratios  $\text{HCN}/\text{HNC} \geq 5$ , however, rules out substantial contributions by shocked or high-temperature gas (cf. Schilke et al. 1992; Hacar et al. 2020).

The analysis by Hacar et al. (2020) also reveals a strong dependence of individual HCN and HNC intensities on gas temperature,  $I(\text{HNC}) \propto T_{\text{k}}$  and  $I(\text{HCN}) \propto T_{\text{k}}^2$ . At any HCN intensity the corresponding molecular gas column density varies by up to an order of magnitude depending on the actual temperature. The authors suggest that these emissivity effects render extra-galactic HCN measurements unreliable as tracers of dense molecular gas content. For the observed HNC/HNC ratios, the PDR models by Meijerink et al. (2007) require molecular gas column densities  $N(\text{H}_2) \lesssim 10^{22} \text{ cm}^{-2}$ .

### 5.5. Most of the lines are sub-thermally excited

In the models by Schilke et al. (1992), relatively modest typical gas densities  $n_{\text{H}} = n(\text{HI}) + 2n(\text{H}_2) \sim 10^4 \text{ cm}^{-3}$  accompany low HCN/HNC ratios. The single-phase LVG models explored by Graciá-Carpio et al. (2008) to explain their  $J=1-0$ ,  $J=3-2$  HCN and  $\text{HCO}^+$  measurements also yield densities  $n(\text{H}_2) \approx 6 \times 10^4 \text{ cm}^{-3}$  as well as abundances  $[\text{HCN}]/[\text{HCO}^+] \approx 6$ . We use the Meijerink et al. (2007) grid of models of gas excitation by UV photons (PDR) and by X-ray photons (XDR) to further investigate the gas density. The observed HCN/ $\text{HCO}^+$  ratios fit the PDR excitation for densities  $n_{\text{H}} \approx (5 - 20) \times 10^4 \text{ cm}^{-3}$  and UV irradiation  $G = (5 - 50) \times 10^3 G_0$ . At the lowest CO luminosities ( $L(\text{CO}) = 10^7 - 10^8 \text{ K km/s pc}^2$ ), the implied densities are at the lower end with low implied irradiation  $G \leq 10^2 G_0$ . The irradiation requirements are much less if other heating mechanisms

<sup>6</sup>  $G_0 = 1.6 \times 10^{-3} \text{ erg cm}^{-2} \text{ s}^{-1}$ , Habing 1968



such as XDR or mechanical heating (Meijerink et al. 2006; Kazandjian et al. 2012, 2015) apply. Their work shows that XDR excitation is unlikely, as also concluded by Pérez-Beaupuits et al. (2007) who suggested similar densities for a small sample of Seyfert galaxies.

Densities  $n_H \approx 5 - 20 \times 10^4$  are above the critical density for HCO<sup>+</sup>(1-0) but just below the critical density for HCN(1-0) and HNC(1-0). They are well below the critical densities for all other transitions of these molecules. All these lines are thus sub-thermally excited. The HCN/CO model ratios from Meierink et al. (2007) suggest that roughly between 5 and 20 per cent of the observed CO intensity originates in the dense gas that radiates in HCN and HCO<sup>+</sup> whereas the remaining 80-95 per cent then comes, as found before, from less dense gas with typical densities  $n_H \approx 10^3 \text{ cm}^{-3}$ .<sup>7</sup> The isotopologue ratio <sup>12</sup>CO/<sup>13</sup>CO is correlated with the dust temperature derived from the far-infrared continuum (Costagliola et al. 2011, and references therein) but not with the temperature of the dense gas derived from the HCN/HNC isomer ratio (Fig. 7). This confirms that most of the CO-emitting gas must be quite distinct from the HCN-emitting gas.

### 5.6. HCN/CO and FIR/CO do not trace dense gas ratio or star formation efficiency

The ground-state HCN/CO and HCN/FIR intensity ratios are largely unrelated to either distance or luminosity.

The intensity ratios FIR/HCN (or FIR/CO) and HCN/CO have been widely portrayed as proxies for star formation efficiency<sup>8</sup> respectively the fraction of molecular gas that resides in dense gas (see e.g. Gao & Solomon 2004b, more recently Tan et al. 2018; Jiménez-Donaire et al. 2019). This assumes that FIR continuum luminosities are directly proportional to star formation rates, and that velocity-integrated CO and HCN line intensities are directly proportional to the column densities of all molecular gas and dense molecular gas, respectively.

Unfortunately, that is not exactly true for CO where factors such as abundance, dynamics, and excitation all contribute to significant individual as well as systematic variations in the relation between line intensity and underlying gas column density (cf. Pety et al. 2017, Israel 2020). Doubts have been expressed to various degrees also on the use of HCN and HCO<sup>+</sup> as reliable mass tracers by several authors (e.g. Papadopoulos et al. 2007, 2012; Krips et al. 2008, Costagliola et al. 2011, Privon et al. 2015, Mills & Battersby (2017), Pety et al. 2017, Graciá-Carpio et al. 2020, Hacar et al. 2020), prompted by considerations of excitation, chemistry, and radiative transfer. Recently, Li et al. (2020a) specifically emphasized the large uncertainties in dense gas mass estimated from a single line transition.

Single dish measurements of galaxies typically cover large areas sampling a wide range of different ISM conditions. Studies simulating such measurements with molecular line surveys of Milky Way areas (e.g. Stephens et al. 2016, Shimajiri et al. 2017, Evans et al. 2020) show that extended sub-thermal emission from marginally dense gas outshines the emission from high-density filaments and clumps. In nearby galaxy centers (e.g.

Circinus galaxy, NGC 4945, M 51, NGC 253, NGC 1808), high  $J=1-0$  HCN/CO ratios occur that are directly ascribable to environmental conditions other than mass (Curran et al. 2001, Matsushita et al. 2015, Walter et al. 2017, Salak et al. 2018). Molecular line intensities are a function of gas properties (chemical abundance, density, opacity) and environmental conditions (irradiation, turbulence, shocks) that dominate chemistry and excitation mechanism. These do not necessarily average out and molecular gas masses are not simple, linear functions of measured line luminosities.

The observational results in this paper emphasize the inconsistency of HCN/CO ratios as an indicator of the dense gas fraction. The variation from galaxy to galaxy is the same at any given intensity or luminosity ratio. No ratio of HCN or HCO<sup>+</sup> to CO or FIR intensity is systematically correlated with the luminosity of a molecular line, with the FIR continuum luminosity, with the observed isotopological ratio  $I(^{12}\text{CO})/I(^{13}\text{CO})$ , or with distance. Nor is there any systematic difference in HCN/CO ratio between normal galaxies, starburst galaxies and AGNs. In the large number of central regions sampled, the near-constancy of the various line ratio averages over a wide range of luminosities is well-established. If, contrary to our assertion, the HCN and CO luminosities were to reliably measure the respective masses of very dense and modestly dense gas, there would still be no relation between the 'dense gas fraction' HCN/CO and such quantities as total molecular gas mass or CO optical depth. The purported dense gas fraction would also be wholly unrelated to surface brightness or surface area covered.

Much the same can be said for the interpretation of the ratios FIR/CO, FIR/HCN, and FIR/HCO<sup>+</sup> as proxies for star formation efficiencies (more correctly: inverse dense-gas-depletion times). The overwhelming lack of correlation between tracers of different gas density and either the FIR luminosity (also noted by Privon et al. 2015 and Li et al. 2021), the FIR-to-HCN ratio, or the FIR-to-CO ratio is counter to what is expected in the case of proxies for star formation rates and efficiencies. It would mean that the star formation process is insensitive to the relative amounts of dense (HCO<sup>+</sup>) and very dense gas (HCN). The star formation efficiency would also be independent of surface area covered or galaxy type, and there would be a surprising lack of any connection between the rate and the efficiency of star formation. Specifically, it would imply the same efficiency of star formation in local low-luminosity galaxies and in very luminous galaxies (LIRGs and ULIRGs) where star formation rates are usually considered to be one or two magnitudes higher. The overall lack of significant correlations between the relevant data strongly implies that the ground-state HCN-to-CO, FIR-to-CO, or FIR-to-HCN intensity ratios are not meaningful as direct proxies for physical quantities such as the fraction of dense gas in the ISM or the efficiency of star formation in galaxy centers. Instead, especially Figs. 4 and 8 suggest that the line intensities of both CO and HCN primarily reflect the excitation of the molecular gas.

### 5.7. The ISM in galaxy centers.

The ISM in galaxy centers is poor in neutral atomic hydrogen (HI) and almost all gas is molecular hydrogen (H<sub>2</sub>). Analysis of the CO and <sup>13</sup>CO emission in various transitions reveals co-existing molecular gas phases distinguished by density and temperature (cf. Israel 2020). If we assume PDR-excitation for the galaxies in this paper, the emission from HCN and HCO<sup>+</sup> originates in molecular gas at average densities not exceeding  $n_H = 5 \times 10^4 - 2 \times 10^5 \text{ cm}^{-3}$ , low average temperatures of  $T_k = 10 - 50$

<sup>7</sup> These are emission fractions, not mass fractions which may be different depending on the excitation of the lines.

<sup>8</sup> FIR/HCN and FIR/CO do not have the dimension of an efficiency factor. Instead, they are the inverse of the time in which the present amount of (dense) gas will be depleted at the present rate of star formation – assuming that far-infrared and molecular line intensities indeed measure what they are purported to do.

K, and very moderate optical depths  $\tau_{CO} = 1 - 5$ . The gas traced by HCN and  $HCO^+$  is itself only a small fraction ( $\leq 20\%$ ) of the molecular gas traced by CO with substantially lower densities of about  $n_H = 10^3 \text{ cm}^{-3}$ , the precise fraction depending on the actual line ratios and the assumed mode of excitation.

Loenen et al. (2008) used HCN, HNC, and  $HCO^+$  line ratios to investigate the excitation mechanism. In addition to the PDR and XDR models from Meijerink et al. (2007), they also considered models with mechanical heating of cloud volumes in addition to PDR surface heating. They found that most of the line ratios from the Baan et al. (2008) sample require PDRs dominated by mechanical heating. The bottom panels in Fig. 7 are the counterparts to Figs. 1 and 2 by Loenen et al. (2008). They exhibit overall similarity but significantly tighter distributions, reflecting the greater accuracy of our more homogeneous and sensitive database. The combined relative intensities of the HCN,  $HCO^+$  and HNC lines conclusively rule out XDR dominating the excitation in all galaxies as well as pure PDR excitation in most galaxies (cf. Meijerink et al. 2007, Loenen et al. 2008). The molecular gas excitation in our sample is almost certainly dominated by mechanical heating. As a consequence, the density and especially the irradiation requirements are relaxed to lower values. Following Kazandjian et al. (2015), average densities are  $n_H = 10^4 - 10^5 \text{ cm}^{-3}$  and the implied average irradiation drops from  $G = 3 \times 10^4 G_0$  to  $G = 3 \times 10^2 G_0$  for mechanical heating fractions  $\alpha$  increasing from 0.1 to 0.5. The decrease by two orders of magnitude reflects the greater efficiency of volume over surface heating.

The relatively low density, low optical depth, and low irradiation of the molecular gas in galaxy centers are characteristic of an ISM not actively engaged in star formation. There is no independent evidence directly and unambiguously linking molecular line intensities such as  $J=1-0$  CO, HCN, or  $HCO^+$  to gas column density or mass. In this paper, we also observed an overall lack of significant correlations between line ratios and properties that could be interpreted as related to large-scale physical processes. Taken together, this forces the conclusion that, in spite of much effort over the last few decades, single-dish molecular line observations allow little more than assumption-driven speculation and are of little use in the quantitative determination of star formation in galaxy centers.

The significant dispersion of measured line intensities and ratios around the average values, typically a factor of three either way, implies different ISM characteristics for different galaxies, including varying gas phase combinations. Individual ISM descriptions surpassing the average treatment given in this paper can be derived from detailed multi-transition, multiple-species radiative transfer modelling. Preliminary examples have already been published, such as M 82 (Loenen et al. 2010), NGC 253 (Rosenberg et al. 2014a), and Arp 299 (Rosenberg et al. 2014b). The results discussed in this paper show that only thus we may hope to identify the actual ISM physics that underlies the observed patterns or lack thereof. Such a more detailed treatment of the galaxies in the present sample is deferred to a subsequent paper.

## 6. Conclusions

1. This paper presents new *IRAM* and *JCMT* observations of 46 bright galaxies in the  $J=1-0$ ,  $J=3-2$ , and  $J=4-3$  transitions of HCN,  $HCO^+$  and HNC. These are complemented by similar observations as well as  $^{12}\text{CO}(1-0)$  and  $^{13}\text{CO}(1-0)$  from published *IRAM* and *JCMT* surveys. The resulting extensive database covers 130 galaxies in HCN(1-0) and  $HCO^+$ (1-0) and 94 galaxies in HNC(1-0). In addition, it includes 12 galaxies in HCN(2-1), about 50 galaxies in HCN(3-2) and  $HCO^+$ (3-2), 25 galaxies in HCN(4-3), and 18 galaxies in HNC(3-2) and  $HCO^+$ (4-3).
2. The observed intensities were normalized to a common resolution of  $22''$  in order to produce meaningful line intensity ratios. The analysis systematically explores luminosity-luminosity relations as well as relations between line ratios, and relations between line ratios and luminosities.
3. As expected from previous work, the  $J=1-0$  HCN,  $HCO^+$ , and HNC luminosities are all linearly related to CO(1-0) and far-infrared (FIR) luminosities. We also find that this is true for the luminosities in the higher transitions of HCN(3-2),  $HCO^+$ (3-2), HCN(3-2), HCN(4-3), and  $HCO^+$ (4-3). Very little can be concluded from this, however, as the luminosity-luminosity relations are essentially trivial because the luminosities are dominated by the variation in distance and not by the physics of the galaxies sampled.
4. Individual galaxy luminosities and line ratios show significant dispersion around the mean in all comparisons, implying significant differences in molecular gas properties between individual galaxies. The dispersion is uncorrelated with luminosity or line ratio and more likely originates in the detailed ISM physics than in systematic large-scale galaxy properties. Analysis of the ISM in individual galaxies is deferred to a later paper.
5. The average normalized HCN and  $HCO^+$  transitions ladders,  $J=(n+1 \rightarrow n)/J=(1-0)$ , as well as the isotopological ratio  $J=1-0 \text{ }^{12}\text{CO}/^{13}\text{CO}$  are positively correlated with CO and FIR luminosity. No other line ratio shows such a clear correlation with luminosity.
6. HCN and  $HCO^+$  have almost equal intensities and behave very similarly across the entire sample. These two molecules trace the same gas, notwithstanding a significant difference in critical density. In AGN-dominated galaxies, ground-state HCN intensities always exceed those of  $HCO^+$ . Suppression of  $HCO^+$  intensity is more likely than the alternative of HCN-enhancement in starburst galaxies.
7. Our radiative transfer models show that only 5 – 20% of the observed CO emission originates in the HCN/ $HCO^+$ -emitting molecular gas. The HCN and  $HCO^+$  emission represents a mixture of dense gas clouds and an undetermined but significant amount of translucent molecular gas. Except for  $HCO^+(1-0)$ , all observed lines are sub-thermally excited.
8. The observed CO, HCN, and  $HCO^+$  emission is not simply related to molecular gas column density or mass. These lines reflect the excitation of the gas, they are affected by the gas opacity and abundance, but they are not reliable mass tracers.
9. The HCN/CO line intensity ratio cannot be used as a proxy for the dense gas fraction, and the FIR/HCN and FIR/CO intensity ratios are also meaningless as proxies for star formation efficiencies or even molecular gas depletion times. Because the molecular lines do not reliably trace mass, comprehensive understanding of star formation requires a more appropriate determination of gas mass.
10. The molecular line emission from galaxy centers rules out a dominant heating contribution by X-rays (XDRs) but is fully consistent with UV-photon heating (PDRs) enhanced by a significant mechanical heating contribution due to turbulence or shocks.
11. The densest molecular gas in the galaxy centers sampled by ground-state HCN and  $HCO^+$  lines has relatively low average kinetic temperatures  $T_{\text{kin}} = 10 - 50 \text{ K}$ , relatively low average densities  $n_H = 10^4 - 10^5 \text{ cm}^{-3}$ , and relatively low

optical depths of only a few. Most of the gas sampled by CO has densities  $n_{\text{H}} \leq 10^3 \text{ cm}^{-3}$ . If the mechanical heating fraction is 50%, the energy input required is only  $G \sim 300 G_0$ .

## Acknowledgements

Most of the JCMT observations were obtained in service mode. I am especially indebted to the *JCMT* operators and observers, who helped to collect the large data base described in this paper.

## References

- Aalto, S., Polatidis, A.G., Hüttemeister, S., & Curran, S.J., 2002, *A&A* 381, 783
- Aladro, R., Martín, S., Riquelme, D., and 8 co-authors, 2015, *A&A* 579, A101
- Baan W.A., Henkel, C., Loenen, A.F., Baudry, A., & Wiklind T., 2008, *A&A* 477, 747
- Bublitz J., Kastner, J.H., Santander-García, V., & Montez, R., 2019, *A&A* 625, A101
- Bublitz J., Kastner, J.H., Hily-Berland, P., and 4 co-authors, 2022, *A&A* 659, A197
- Bussman, R.S., Narayanan, D., Shirley, Y.L., and 6 co-authors, 2008, *ApJL* 681, L73
- Butterworth, J., Holdship, J., Viti, S., & García-Burillo, S., 2022, *A&A* in press (arXiv:2209.05928)
- Curran, S.J., Johansson, L.E.B., Bergman, P., Heikkilä, A., & Aalto, S., 2001, *A&A* 567, 467
- Costagliola, F., Aalto, S., Rodríguez, M.I., and 10 co-authors, 2011, *A&A* 528, A30
- Evans, N.J., 1999, *ARAA* 37, 311
- Evans, N.J., Kim, K.-T., Wu, J., and 5 co-authors, 2020, *ApJ* 894, 103
- Gao, Y., & Solomon, P.M., 2004a, *ApJS* 152, 63
- Gao, Y., & Solomon, P.M., 2004b, *ApJ* 606, 271 (GS04)
- García-Burillo, S., Usero, A., Alonso-Herrero, A., and five co-authors, 2012, *A&A* 539, A8
- Graciá-Carpio, J., García-Burillo, S., Planesas, P., & Colina, L., 2006, *ApJL* 640, L135
- Graciá-Carpio, J., García-Burillo, S., Planesas, P., Fuente, A., & Usero, A., 2008, *A&A* 479, 703
- Graciá-Carpio, J., 2009, PhD Thesis, Univ. Autónoma de Madrid (E)
- Graninger, D.M., Herbst, E., Öberg, K.I., & Vasyunin, A.I., 2014, *ApJ* 787, 74
- Green, C.-E., Cunningham, R.M., Green, J.A., and 7 co-authors, 2016, *MNRAS* 457, 2470
- Habing, H. J., 1968, *Bull. Astr. Netherlands* 19, 421.
- Hacar, A., Bosman, A.D., & Van Dishoeck, E.F., 2020, *A&A* 635, A4
- Herrero-Illana, R., Privon, G.C., Evans, A.S., and 22 co-authors, 2019 *A&A* 628, A71
- Hüttemeister, S., Henkel, C., Mauersberger, R., Brouillet, N., Wiklind, T., & Mil-lar, T.J., 1995, *A&A* 295, 571
- Imanishi, M., Nakanishi, K., Tamura, Y., & Kohno, K., 2007, *AJ* 134, 2366
- Imanishi, M., 2009, *ApJ* 694, 751
- Imanishi, M., Nakanishi, K., & Izumi, T., 2016, *AJ* 152, 218
- Imanishi, M., Nakanishi, K., & Izumi, T., 2018, *ApJ* 856, 143
- Imanishi, M., Nakanishi, K., & Izumi, T., 2019, *ApJS* 241, 19
- Imanishi, M., Nakanishi, K., Izumi, T., & Baba, S., 2022, *ApJ* 926, 159
- Israel, F.P., 2020, *A&A* 635, A131 (Paper I)
- Izumi, T., Kohno, K., Aalto, S., and 16 co-authors, 2016, *ApJ* 818, 42
- Izumi, T., Nguyen, D.D., Imanishi, M., and 15 co-authors, 2020, *ApJ* 898, 75
- Jansen, D.J., 1995, PhD Thesis, Leiden University
- Jiang, X., Wang, J., & Gu, Q., 2011, *MNRAS* 418, 1753
- Jiménez-Donaire, M.J., Bigiel, F., Leroy, A.K., and 17 co-authors, 2017, *MNRAS* 466, 49
- Jiménez-Donaire, M.J., Bigiel, F., Leroy, A.K., and 14 co-authors, 2019, *ApJ* 880, 127
- Jones, P.S., Burton, M.G., Cunningham, R.M., and 8 co-authors, 2012, */mnras* 419, 2961
- Kazandjian, M., Meijerink, R., Pelupessy, F.I., Israel, F.P., & Spaans, M., 2012, *A&A* 542, A65
- Kazandjian, M., Meijerink, R., Pelupessy, F.I., Israel, F.P., & Spaans, M., 2015, *A&A* 574, A127
- Kazandjian, M., Meijerink, R., Pelupessy, F.I., Israel, F.P., & Spaans, M., 2016, *A&A* 595, A125
- Kennicutt, R., 1990, in *The Interstellar Medium in Galaxies*, eds. Thronson & Shull (Dordrecht: Kluwer), p. 405
- Knudsen, K.K., Walter, F., Weiss, A., and 3 co-authors, 2007, *ApJ* 666, 156
- Kohno, K., Matsushita, S., Vila-Vilaró, B., and 5 co-authors, 2001, in “The Central Kiloparsec of Starbursts and AGN” ASP Conf. Proc., 249, 672
- Krips, M., Neri, R., García-Burillo, S., and 4 co-authors, 2008, *ApJ* 677, 262
- Li, F.-C., Wu, Y.-W., & Xu, Y., 2015, *Res. Astron. Astrophys.*, 15, 785
- Li, F., Wang, J., Kong, M., & Li, S., 2019, *MNRAS* 482, 4763
- Li, F., Wang, J., Fang, M., and 4 co-authors, 2020a *PASJ* 72, 41
- Li, F., Wang, J., Fang, M., and 4 co-authors, 2020b *MNRAS* 494, 1095
- Li, F., Wang, J., Gao, F., and 6 co-authors, 2021, *MNRAS* 503, 4508 (L121)
- Loenen, A.F., Spaans, M., Baan, W.A., & Meijerink, R., 2008, *A&A* 488, L5
- Loenen, A.F., van der Werf, P.P., Güsten, R. and 23 co-authors, 2010, *A&A* 521, L2
- Matsushita, S., Dinh-V-Trung, Boone, F., Krips, M., Lim, J., & Muller, S., 2015, *ApJ* 799, 26
- Meijerink, R., Spaans, M., & Israel, F. P., 2006, *ApJL* 650, L103
- Meijerink, R., Spaans, M., & Israel, F. P., 2007, *A&A* 461, 793
- Mills, E.A.C., & Basttersby, C., 2017, *ApJ* 835, 76
- Nguyen-Q-Rieu, Jackson, J.M., Henkel, C., Truong-Bach, & Mauersberger, R., 1992, *ApJ* 399, 521
- Papadopoulos, P.P., 2007, *ApJ*, 656, 792
- Papadopoulos, P.P., van der Werf, P., Xilouris, M., Isaak, K.G., & Gao, Y., 2012, *ApJ* 751, 10
- Pérez-Beaupuits, J.P., Aalto, S., & Gerebro, H., 2007, *A&A* 476, 177
- Pey, J., Guzmán, V.V., Orkisz, J.H., and 11 co-authors, 2017, *A&A* 599, A98
- Privon, G.C., Herrero-Illana, R., Evans, A.S., and 18 co-authors, 2015 *ApJ* 814, 39
- Privon, G.C., Ricci, C., Aalto, S., and 18 co-authors, 2020 *ApJ* 893, 149
- Romano, D., Matteucci, F., Zhang, Z.-Y., Papadopoulos, P.P., & Ivison, R.J., 2017, *MNRAS* 470, 401
- Rosenberg, M.J.F., Kazandjian, M.V., van der Werf, P.P., and 5 co-authors, 2014a, *A&A* 564, A128
- Rosenberg, M.J.F., Meijerink, R., Israel, F.P., and 3 co-authors, 2014b, *A&A* 568, A90
- Sage, L.J., Henkel, C., & Mauersberger, R., 1991, *A&A* 249, 31
- Salak, D., Tomiyasu, Y., Nakai, N., Kuno, N., Miyamoto, Y., & Kaneko, H., 2016, *ApJ* 856, 97
- Schilke, P., Walmsley, C.M., Pineau-des-Forêts, G., and 3 co-authors, 1992, *A&A* 256, 595
- Shimajiri, Y., André, Ph., Braine, J., and 7 co-authors, 2017, *A&A* 604, A74
- Shirley, Y.L., 2015, *PASP* 127, 299
- Solomon, P.M., Radford, S.J.E., & Downes D., 1992, *Nature*, 356, 318
- Stephens, I.W., Jackson, J.M., Whitaker, J.S., and 5 co-authors, 2016, *ApJ* 824, 29
- Tan, Q.-H., Gao, Y., Zhang, Z.-Y., and 46 co-authors, 2018, *ApJ* 860, 165
- Visser, R., Van Dishoeck, E.F., & Black, J.H., 2009, *A&A* 503, 323
- Viti, S., Fontani, F., & Jiménez-Serra, I., 2020, *MNRAS* 497, 4333
- Walter, F., Bolatto, A.D., Leroy, A.K., and 12 co-authors, 2017, *ApJ* 835, 265
- Wilson T.L., 1999, *Rep. Prog. Phys.*, 62, 143
- Zhang, Z.-Y., Gaom Y., Henkel, C., and 4 co-authors, 2014, *ApJL* 784, L31
- Zhou, J., Zhang, Z.-Y., Gao, Y., and 6 co-authors, 2022, *ApJ* 936, 58